Fig. 3. Effects of TBC1D1 knockdown on primary rat beta-cell function. (A) Representative Western blot and quantification showing efficiency of TBC1D1 knockdown in rat primary beta-cells (n = 3). (B) Glucose stimulated insulin secretion. Beta-cells were incubated for 60 min at 2.8 mmol/l glucose (open bars) followed by 60 min at 16.7 mmol/l glucose (closed bars) (n = 5) *P < 0.05 as tested by ANOVA followed by Bonferroni post hoc test. (C) KCl stimulated insulin secretion. Beta-cells were incubated for 60 min at 2.8 mmol/l glucose (open bars) followed by 10 min at 30 mM KCl (striated bars) (n = 3).
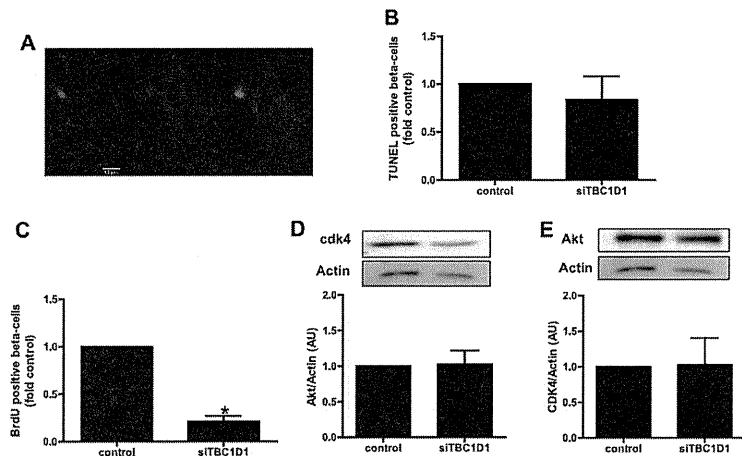
Fig. 4. Effects of TBC1D1 knockdown on beta-cell turnover. (A) Representative images of primary rat sorted beta-cells co-stained for TUNEL (red), insulin (green) and nuclei (blue). (B) Effect of knockdown of TBC1D1 on rat primary beta-cell death measured by TUNEL (n = 5). (C) Effect of TBC1D1 knockdown on rat primary beta-cell proliferation. Proliferation was measured by BrdU incorporation over 24 h (n = 6). *P < 0.05 vs control siRNA by Student's t test. (D and E) Representative Western blot and quantification of Akt (D) and Cdk4 (E) after knockdown of TBC1D1 (n = 4).

observed between Glut4 and insulin vesicle trafficking [16]. We report here for the first time that two key TBC1D1 phosphorylation sites, Ser-231 (AMPK dependent) and Thr-596 (probably Akt dependent), are phosphorylated in response to glucose, suggesting that TBC1D1 is implicated in the beta-cell function. However, Ser-231 is phosphorylated already after 10 min glucose stimulation, whereas Thr-596 is only phosphorylated after 1 h of stimulation. The kinetics of phosphorylation of the 2 phospho-specific sites in response to glucose suggests either that TBC1D1 interacts with different kinases or that different stimuli are involved (glucose vs insulin/IGF2). Our data suggest that AMPK and Akt are involved in the early (Ser-231) and late (Thr-596) glucose-stimulated TBC1D1 phosphorylation events respectively. It is postulated that downstream signalling cascades may impact differently on beta-cell function. These cascades are multiple, complex and overlapping, both in terms of insulin secretion [17] and beta-cell proliferation [18] which make their identification complex.

In insulin target tissues, TBC1D1 and AS160/TBC1D4 phosphorylation inhibits their Rab-GAP activity. Therefore, silencing of TBC1D1 mimics this phosphorylation and inactive status. Knockdown of TBC1D1 mildly affected beta-cell function by increasing to a small and comparable extent both basal and stimulated insulin secretion, while we have shown that AS160/TBC1D4 was a key regulator of insulin secretion [4]. This suggests that TBC1D1 might interact with specific Rab proteins distinct from those downstream of TBC1D4. Moreover, beta-cells with decreased TBC1D1 expression were unable to respond to KCl stimulated insulin secretion. Overall, our results suggest that TBC1D1 gets phosphorylated in response to glucose stimulation in beta-cells without playing a major role in glucose stimulated insulin release. However, it appears essential for calcium mediated insulin release in response to direct depolarization by KCl. The apparent discrepancy between these findings is perhaps explained by the well-documented ability of glucose to elicit insulin secretion through increased cytosolic calcium while also activating a calcium-independent potentiating pathway [19] that would appear not to require TBC1D1. In summary, our data suggest that the 2 paralog proteins, TBC1D1 and 4, have distinct roles in the regulation of insulin secretion; TBC1D1 plays a role in the maintenance of baseline insulin secretion and is essential for calcium-mediated secretion, whereas AS160/TBC1D4 plays a more central role in glucose stimulated insulin secretion.

Decreased protein expression of TBC1D1 inhibited beta-cell proliferation without affecting survival, while AS160/TBC1D4 is involved in both beta-cell survival and proliferation suggesting again that these 2 proteins have non-redundant functions [4]. The strong decrease in beta-cell proliferation when TBC1D1 is knocked down seems to be independent of the glucose concentration present in the media, suggesting that TBC1D1 plays a central role in beta-cell proliferation. However, when looking at the expression of proteins involved in beta-cell survival and in the cell cycle, knockdown of TBC1D1 does not influence their expression. Nevertheless, TBC1D1 might interact with protein complexes involved in the regulation of the cell cycle.

In conclusion, this study reports for the first time that TBC1D1, known to be involved in the insulin response in muscle and adipose tissue, is expressed in beta-cells, is phosphorylated in response to glucose and is involved in beta-cell proliferation and insulin release.

5. Author contributions

S.R., P.A.H. and K.B. designed experiments. M.K. generated reagents. S.R., C.A., A.C.N. and K.B. performed experiments. S.R., P.A.H. and K.B. wrote and edited the manuscript.

References

[1] Kido, Y., Burks, D.J., Withers, D., Bruning, J.C., Kahn, C.R., White, M.F. and Accili, D. (2000) Tissue-specific insulin resistance in mice with mutations in the insulin receptor, IRS-1, and IRS-2. J. Clin. Invest. 105, 199–205.
[2] Assmann, A., Hinault, C. and Kulkarni, R.N. (2009) Growth factor control of pancreatic islet regeneration and function. Pediatr. Diabetes 10, 14–32.
[3] Sakamoto, K. and Holman, G.D. (2008) Emerging role for AS160/TBC1D4 and TBC1D1 in the regulation of GLUT4 traffic. Am. J. Physiol. Endocrinol. Metab. 295, E29–37.
[4] Bouzakri, K., Ribaux, P., Tomas, A., Parnaud, G., Rickenbach, K. and Halban, P.A. (2008) Rab GTPase-activating protein AS160 is a major downstream effector of protein kinase B/Akt signaling in pancreatic beta-cells. Diabetes 57, 1195–1204.
[5] Kane, S., Sano, H., Liu, S.C., Asara, J.M., Lane, W.S., Garner, C.C. and Lienhard, G.E. (2002) A method to identify serine kinase substrates. Akt phosphorylates a novel adipocyte protein with a Rab GTPase-activating protein (GAP) domain. J. Biol. Chem. 277, 22115–22118.
[6] Szekeres, F., Chadt, A., Tom, R.Z., Deshmukh, A.S., Chibalin, A.V., Bjornholm, M., Al-Hasani, H. and Zierath, J.R. (2012) The Rab-GTPase-activating protein TBC1D1 regulates skeletal muscle glucose metabolism. Am. J. Physiol. Endocrinol. Metab. 303, E524–533.
[7] Chadt, A., Leicht, K., Deshmukh, A., Jiang, L.Q., Scherneck, S., Bernhardt, U., Dreja, T., Vogel, H., Schmolz, K., Kluge, R., Zierath, J.R., Hultschig, C., Hoeben, R.C., Schurmann, A., Joost, H.G. and Al-Hasani, H. (2008) Tbc1d1 mutation in lean mouse strain confers leanness and protects from diet-induced obesity. Nat. Genet. 40, 1354–1359.
[8] Roach, W.G., Chavez, J.A., Miinea, C.P. and Lienhard, G.E. (2007) Substrate specificity and effect on GLUT4 translocation of the Rab GTPase-activating protein Tbc1d1. Biochem. J. 403, 353–358.
[9] Pehmoller, C., Treebak, J.T., Birk, J.B., Chen, S., Mackintosh, C., Hardie, D.G., Richter, E.A. and Wojtaszewski, J.F. (2009) Genetic disruption of AMPK signaling abolishes both contraction- and insulin-stimulated TBC1D1 phosphorylation and 14-3-3 binding in mouse skeletal muscle. Am. J. Physiol. Endocrinol. Metab. 297, E665–675.
[10] Hatakeyama, H. and Kanzaki, M. (2013) Regulatory mode shift of Tbc1d1 is required for acquisition of insulin-responsive GLUT4-trafficking activity. Mol. Biol. Cell 24, 809–817.
[11] Cousin, S.P., Hugl, S.R., Wrede, C.E., Kajio, H., Myers Jr., M.G. and Rhodes, C.J. (2001) Free fatty acid-induced inhibition of glucose and insulin-like growth factor I-induced deoxyribonucleic acid synthesis in the pancreatic beta-cell line INS-1. Endocrinology 142, 229–240.
[12] Parnaud, G., Bosco, D., Berney, T., Pattou, F., Kerr-Conte, J., Donath, M.Y., Bruun, C., Mandrup-Poulsen, T., Billestrup, N. and Halban, P.A. (2008) Proliferation of sorted human and rat beta cells. Diabetologia 51, 91–100.
[13] Bouzakri, K., Ribaux, P. and Halban, P.A. (2009) Silencing mitogen-activated protein 4 kinase 4 (MAP4K4) protects beta-cells from TNF-alpha induced decrease of IRS2 and inhibition of glucose-stimulated insulin secretion. J. Biol. Chem. 284 (41), 27892–27898.
[14] Nica, A.C., Ongen, H., Irminger, J.C., Bosco, D., Berney, T., Antonarakis, S.E., Halban, P.A. and Dermitzakis, E.T. (2013) Cell-type, allelic and genetic signatures in the human pancreatic beta cell transcriptome. Genome Res. 23 (9), 1554–1562.
[15] Gaidhu, M.P., Perry, R.L., Noor, F. and Ceddia, R.B. (2010) Disruption of AMPKalpha1 signaling prevents AICAR-induced inhibition of AS160/TBC1D4 phosphorylation and glucose uptake in primary rat adipocytes. Mol. Endocrinol. 24, 1434–1440.
[16] Hou, J.C., Min, L. and Pessin, J.E. (2009) Insulin granule biogenesis, trafficking and exocytosis. Vitam. Horm. 80, 473–506.
[17] Henquin, J.C. (2009) Regulation of insulin secretion: a matter of phase control and amplitude modulation. Diabetologia 52, 739–751.
[18] Kulkarni, R.N., Mizrachi, E.B., Ocana, A.G. and Stewart, A.F. (2012) Human beta-cell proliferation and intracellular signaling: driving in the dark without a road map. Diabetes 61, 2205–2213.
[19] Henquin, J.C. (2011) The dual control of insulin secretion by glucose involves triggering and amplifying in beta-cells. Diabetes Res. Clin. Pract. 93 (Suppl. 1), S27–31.

Self-activated mesh device using shape memory alloy for periosteal expansion osteogenesis

Kensuke Yamauchi,[1] Tetsu Takahashi,[1] Kenko Tanaka,[1] Shinnosuke Nogami,[2] Takeshi Kaneuji,[2] Hiroyasu Kanetaka,[3] Toshiki Miyazaki,[4] Bernd Lethaus,[5] Peter Kessler[5]

[1]Division of Oral and Maxillofacial Surgery, Tohoku University Graduate School of Dentistry, Sendai, Japan
[2]Division of Oral and Maxillofacial Reconstructive Surgery, Kyushu Dental College, Kitakyushu, Japan
[3]Laison Center for Innovative Dentistry, Graduate School of Dentistry, Sendai, Japan
[4]Department of Biological Functions and Engineering, Graduate School of Life Science and Systems Engineering, Kyushu Institute of Technology, Kitakyushu, Japan
[5]Department of Cranio-Maxillofacial Surgery, Maastricht University Medical Center, Maastricht, The Netherlands

Abstract: The present study evaluated the use of this self-activated shape memory alloy (SMA) device, with a focus on its effects in the region under the periosteum. Twelve Japanese white rabbits were used in this study. The device was inserted under the periosteum at the forehead. In the experimental group, the device was pushed, bent, and attached to the bone surface and fixed with a titanium screw. In control group, the device was only inserted under the periosteum. After 14 days, the screw was removed and the mesh was activated in the experimental group. Rabbits were sacrificed 5 and 8 weeks after the operation and newly formed bone was histologically and radiographically evaluated. The quantitative data by the area and the occupation of newly formed bone indicated that the experimental group had a higher volume of new bone than the control group at each consolidation period. Histologically, some newly formed bone was observed and most of the subperiosteal space underneath the device was filled with fibrous tissue, and a thin layer of immature bone was observed in the control group. In the experimental group, multiple dome-shaped bones, outlined thin and scattered trabeculae, were clearly observed under the SMA mesh device. The use of self-activated devices for the periosteal expansion technique may make it possible to avoid donor site morbidity, trans-skin activation rods, any bone-cutting procedure, and the following intermittent activation procedure. © 2013 Wiley Periodicals, Inc. J Biomed Mater Res Part B: Appl Biomater 101B: 736–742, 2013.

Key Words: animal model, bone graft, maxillofacial, osteogenesis

INTRODUCTION

Alveolar bone augmentation is one of the standard treatments for dental implantation when alveolar bone volume is insufficient. A relevant vertical and/or horizontal defect of the alveolar ridge is still a challenge for appropriate implant placement and predictable long-term results.
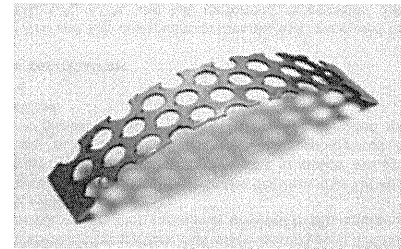
Autogenous bone grafting is considered the gold standard for maxillofacial bone reconstruction.[1,2] However, this technique may be associated with donor site morbidity and resorption of the grafted bone, and it cannot be used for simultaneous soft tissue augmentation. Thus, the amount of bone augmentation is usually limited.

In contrast, distraction osteogenesis (DO) is an alternative method that uses a biological process in which new bone formation occurs between segments that are gradually separated.[3,4] This gradual traction of pedicled bone fragments is followed by simultaneous osteogenesis (bone) and histogenesis (functional soft tissue matrix). However, disagreement exists regarding the various treatment parameters, such as surgical technique, type of distraction device, and minimal bone height and width necessary to perform distraction.

Recently, osteogenesis by periosteal distraction or elevation without corticotomy for bone augmentation has been suggested.[5–9] This method is based on the concept that tensile strain on the periosteum, which causes tenting of the subperiosteal capsule, is sufficient to produce bone formation, without corticotomy or local harvesting of the bone. These studies indicated a new technical aspect of DO or tissue expansion, with the controlled guided formation of new bone.

Previously, we investigated the utility of periosteal expansion osteogenesis (PEO), the same concept as periosteal DO or elevation, using a highly purified β-tricalcium phosphate (β-TCP) block, instead of titanium devices, in a dog model. We found that newly formed bone at the gap between the original bone and β-TCP block, and the β-TCP block, acted as a space-maker under the periosteum. This suggests the possibility to inducing newly formed bone with no autogenous grafting or osteotomy. However, it needs mechanical activation, as does a DO protocol with a turning device penetrating the mucosa or skin. Such penetration of soft tissue around the augmented area can cause wound dehiscense or exposure of the device, and subsequent infection. Considering the ideal conditions for acquiring sufficient bone, a complete capsule under the periosteum is required.

Many studies have done to make novel distraction device that expand automatically and automatically, for example motor-driven, spring-mediated and hydraulic devices.[10] However most of those devices were too big to implantation. Clinical useful device that has an automated activity require specific parameters; small size, easily implantable, fully buried,biocompatible, sufficient force generation and maintenance. NiTi implants have been used for cardiovascular and orthodontic treatments.[11,12] However these materials are not used for bone augmentation, although a few animal studies have shown the possibility of using them for jaw elongation or alveolar bone augmentation with a DO technique. And those were used as spring device, so it is difficult to control the activation rhythm and distraction or expansion vector. To create the ideal space with no manual activation, we developed a simple self-activated mesh device made of Ni-Ti shape-memory alloy (SMA) for periosteal expansion. The present study evaluated the use of this self-activated using SMA device with a forcus on its effects in the region under the periosteum.

Correspondence to: K. Yamauchi; e-mail: yamaken29@gmail.com

FIGURE 1. Image of SMA device. [Color figure can be viewed in the online issue, which is available at wileyonlinelibrary.com.]

MATERIALS AND METHODS

Japanese white rabbits (all male, 3–3.5 kg) were used and were divided into four groups of three according to the time of sacrifice and with or without activation. The protocol and guidelines for this study were approved by the Institutional Animal Care and Use Review Committee of Kyushu Dental College, Kitakyushu, Japan.

In the control group, the device was only inserted with no activation, and others in the experimental groups, it was inserted and activated after a latency period. Groups were also defined for consolidation periods of 5 and 8 weeks after surgery.

Device description

The device consisted of Ni-Ti materials (Ni; 56.1, Ti; balance, Fe; ≤ 0.05, O; ≤ 0.05, C; ≤ 0.03, N; ≤ 0.02, wt %). The form of the mesh device was 5-mm width, 25-mm length, and 0.275-mm thickness. The pre-curved form was designed that the middle point was 4-mm above from the baseline (Figure 1).

The deformation behavior of the SMA mesh plate was measured by a compressive test (Figure 2). The plate was fixed on an Instron-type testing machine (Model AG-I; Shimadzu, Japan), and compressive stress was applied perpendicularly to the plate at a cross-head speed of 1.0 mm min^{-1}. Compressive load (σ) and displacement (l) was calculated when the plate became completely flat.
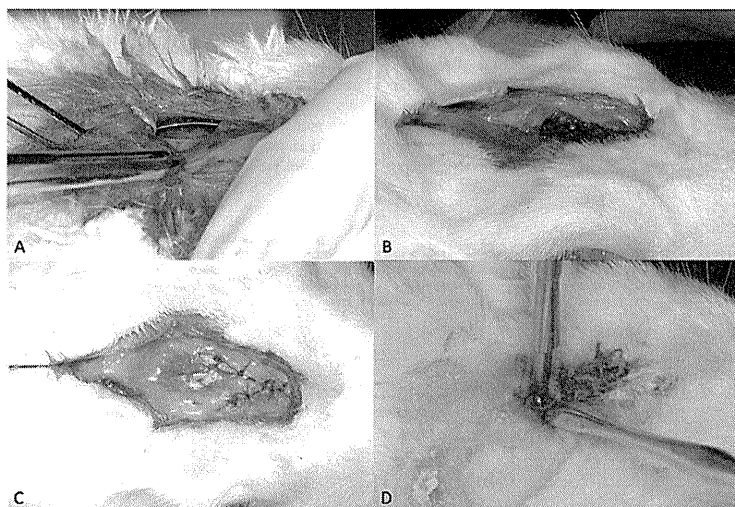
Surgical protocol

The animals were anesthetized by intramuscular administration of ketamine hydrochloride (60 mg kg^{-1} Ketalar; Sankyo, Tokyo), followed by diazepam (5 mg) and atropine sulfate (0.5 mg), without endotracheal intubation. Before the operation, 10 mg kg^{-1} pentobarbital sodium was injected intravenously. In addition, 1.8 mL of local anesthetic (2% xylocaine and epinephrine 1:80,000, Dentsply Sankin, Tokyo, Japan) was used during all surgical procedures. Immediately after the operation, the animals received cefazolin sodium (20 mg kg^{-1}) subcutaneously, which was continued until postoperative day 3.

The operation was performed under standard sterile conditions. The forehead of the animal was shaved and disinfected with 1% iodine sodium. After a U-shaped skin and V-shaped periosteal incisions were made in the forehead region, the frontal bone of the animal was exposed following the careful elevation of the periosteum. The device was inserted under the periosteum [Figure 3(A)]. In the experimental group, the device was pushed, bent, and attached to
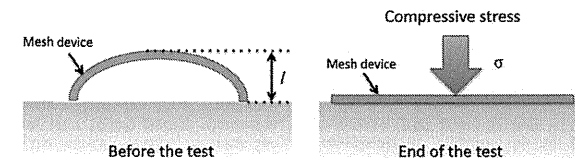
FIGURE 2. Scheme of the compressive test. σ: Compressive load; l: displacement. [Color figure can be viewed in the online issue, which is available at wileyonlinelibrary.com.]

FIGURE 3. Image of surgical procedure. SMA device under periosteum (A), fixation with titanium screw at the bended position (B). Closure with periosteum over the device (C). Image at the screw removal after latency period for 2 weeks (D). [Color figure can be viewed in the online issue, which is available at wileyonlinelibrary.com.]

the bone surface and fixed with a titanium screw (diameter: 2.0 mm, length 4 mm) [Figure 3(B)]. In control group animals, the device was only inserted under the periosteum. After irrigation with saline, the periosteum was positioned back in its original place and stabilized by suturing with 5-0 Vicryl. The skin was made using 4-0 Vicryl [Figure 3(C)].

Postoperative protocol
All rabbits were given water and normal rabbit food postoperatively. After 14 days a soft tissue incision of 2-mm long was made over the screw and a driver was inserted for its removal of it in the experimental group [Figure 3(D)]. The wound was closed using 5-0 Vicryl after screw removal in the experimental group. Rabbits were sacrificed after a 3- and 6-week consolidation period with a lethal dose of thiopental sodium. In control group, the timing of the sacrifice was the same as in the experimental group, so it was done at 5 and 8 weeks after the operation. The cranial bone was removed and fixed for 14 days in 10% buffered formalin.

Tissue preparation and histological evaluation
Cranial bone tissue was evaluated by soft focused X-ray CT (Comscantechno, Yokohama, Japan) under electrical conditions of 65 µA and 70 kV. Measurements were made on three vertical images per specimen, closest to the center of the device. In each image, the area occupied by the new bone was measured using image analysis software (Image J, ver.1.44; NIH, Bethesda, MD). The complete area underneath the SMA device was defined as "the expanded volume" (EV).

The area of mineralized tissue in the EV was defined as "the total bone volume" (TBV). The percentage ratio of EV/TBV was calculated to assess the extent of new bone growth.

Specimens were fixed without decalcification and then immersed in Villanueva bone stain solution (Maruto, Tokyo, Japan). Then the specimens were then dehydrated through a graded ethanol series, embedded in methylmethacrylate (Wako Pure Chemical Industries, Osaka, Japan), and cut in 5-µm sections (Exact, Mesmer, Ost Einbeck, Germany).

Statistical analysis
Statistical analyses were performed using the SPSS software (ver. 10.0; SPSS, Chicago, IL). Normality and homogeneity were analyzed with variance tests. A paired t test was used to analyze the area of newly formed bone and the ratio of EV/TBV of all groups. The level of significance was chosen in all statistical tests was set at $p < 0.01$.

RESULTS
Average compressive load and displacement was summarized in Table I. Width of the center and the whole of the

TABLE 1. Average Compressive Load and Strain of Whole the Plate and Center of the Plate (n = 3)

	Compressive Load (σ)/N	Displacement (1)/mm
Whole the plate	4.2	3.99
Center of the plate	0.9	4.05
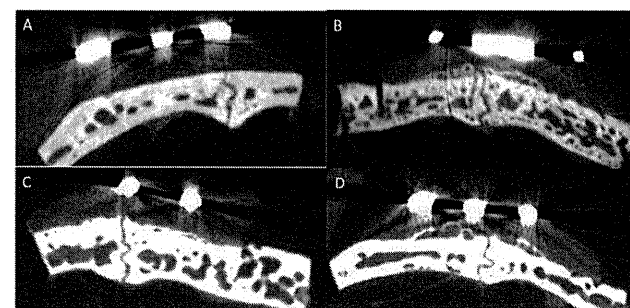
FIGURE 4. Soft focused X ray CT images showing cross sectional view of few bone over the original bone at postoperative 5 weeks in control group (A). Dome shape bone outlined from original bone was observed at postoperative 5 and 8 weeks in the experimental group (B–D). A thin newly formed bone was observed on the original bone at postoperative 8 weeks in control group (D).

plate are 5 and 15 mm, respectively. If it is assumed that the former has the same size as the latter, compressive load required for the same displacement as the latter is calculated as 2.7 N (= 0.9 ÷ 5 × 15). This is lower than the measured compressive load of whole the plate. This is attributed to the face that the center of the plate has porous structure.

No complications related to the materials used at the sites of intervention, before, during, or at the end of the experimental phase or infection within or around the device were observed in any animal. Upon screw removal, the device was activated to the original position immediately in two animals. They were concealed under the soft tissue during activation and the consolidation period until the time of sacrifice and no clinically active inflammation was observed around the SMA device.

Five and eight weeks after operation, soft focused X-ray CT images showed that the newly formed bone was less radiopaque than the original bone. Newly formed bone tissue was hardly observed in the control group at postoperative 5 weeks. The peak of newly formed bone was located under the center of the device [Figure 4(A)]. The dome shape bone outlined from original bone in the experimental group [Figure 4(B,D)]. The quantitative data by the area and the occupation of newly formed bone (TBV/EV) indicated that the experimental group had a higher volume of new bone than the control group at each consolidation period ($p < 0.01$) (Table II). With increasing bone consolidation period, the date was also relatively increased but there were no static difference between both of time course.

Five weeks after operation, some newly formed bone was observed and most of the subperiosteal space underneath the device was filled with fibrous tissue with no inflammatory cell reaction, and a thin layer of immature bone was observed at the outer surface of original skull bone in the control group [Figure 5(A)]. In the experimental group, a thin osteogenic layer, same as in the control group, was also observed along with an obvious, prominent, newly formed bone trabeculae connecting the layer to the original bone [Figure 5(B)].

Eight weeks post-operation, similar histological patterns were observed in the control group [Figure 5(C)]. A layer of immature bone and a bridge-like structure were observed. However, quantitative evaluations showed no difference between them in the time course. In the experimental group, multiple dome-shape bones, outlined by thin and scattered bone trabeculae were clearly observed under the SMA mesh device [Figure 5(D)]. These newly formed bone trabeculae were observed in the center of the SMA device, and the domed shape of the newly formed bone trabeculae was similar to the curved shape of the SMA device in some specimens.

DISCUSSION
DO is successful because, under appropriate levels of stimulation, periosteal mesenchymal stem cells differentiate into osteoblasts and produce an early subperiosteal callus within the osteomized gap.[13,14] The most recent concept of periosteal DO is also based on the potential of the periosteum to differentiate into osteoblasts to fill the space over the underlying bone.

TABLE 2. Table Showing the Quantitative Data by the Area and the Occupation of Newly Formed Bone (TBV/EV)

	Postope 5 Weeks (Mean ± SD)		Postope 8 Weeks (Mean ± SD)	
	Control	Experiment	Control	Experiment
Bone area (mm2)	0.10 ± 0.12	2.14 ± 0.85	0.34 ± 0.18	2.90 ± 1.13
Ratio of TBV/EV (%)	1.6 ± 1.1	27.3 ± 10.8	11.2 ± 4.5	31.1 ± 12.1

*$p < 0.01$
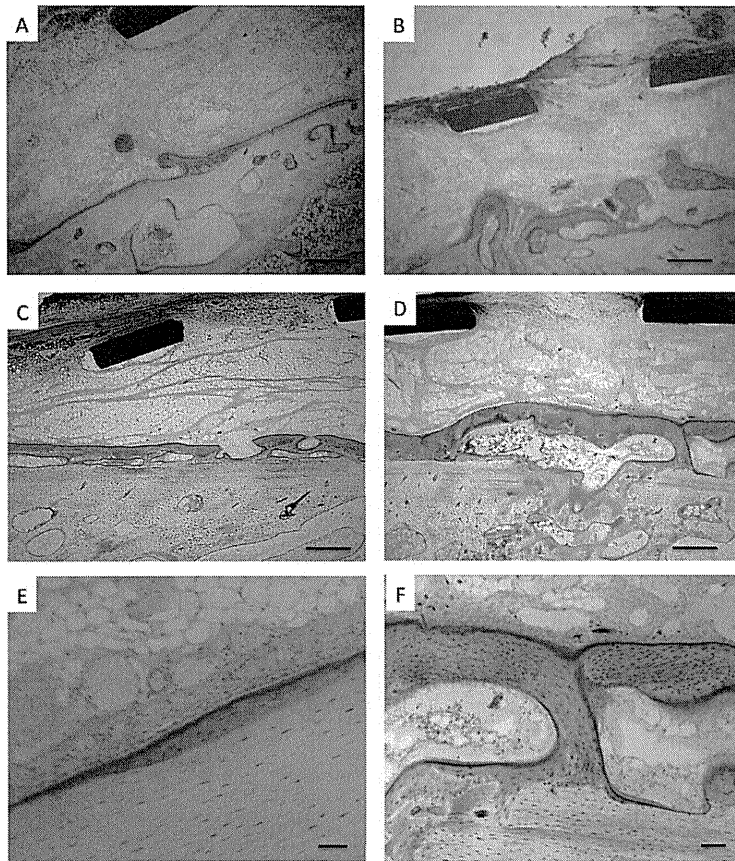
FIGURE 5. Representative histological images stained with Villanueva bone stain for control and experimental group Scale = 300μin A,B,C,D, 30μin E,F. A thin newly formed bone layer was seen over the original bone at postoperative 5 weeks in control group (A). A prominent newly formed bone connected with thin layer same as (A) was observed at postoperative 5 weeks in the experimental group (B). A layer of newly formed bone and some bridge-like structure was observed at postoperative 8 weeks in control group (C). A multiple dome shape bone was observed at postoperative 8 weeks in the experimental group (D).

Previous reports of periosteal DO showed new bone formation in the gap created by the devices. However the disadvantages for clinical application still exist. One is that most devices penetrate the skin or mucosa and need manual mechanical activation to create the space between the periosteum and underlying bone. It is also difficult to close the wound with the periosteum over a bulky device. Sufficient closure with the periosteum is an important factor to acquire newly

formed bone as a result of periosteal DO. The device used in this study consisted of a thin NiTi mesh device (0.25mm thick) and had the advantage of acquiring an ideal capsule under the periosteum. This thin SMA device can be used as an automated and fully internalized distraction device, which might resolve many complications with minimal invasion.

The histological findings demonstrated that newly formed bone originated mainly from the underlying original

bone. Even in the control group, a thin layer of immature bone was observed at the surface of the bone. It seemed that progenitor cells were from the blood and osteoblasts were provided from the original bone. In addition, the prominent newly formed bone under the device was observed in the experimental group. The location of the main prominence was at the same level as the mid point of the device. It seemed that the pressure from the overlying soft tissue affected the ossification from the original bone and the excess tension under the periosteum prevented the production of newly formed bone. However, Zakaria et al. reported that the relatively thick trabecular bone was observed in the segment near to fixed end.[9] In this study, newly formed bone was observed more in the middle part than at the end. A fixation screw was placed in the center of the device and removed after a latency period of 2 weeks, so the end of the device was not fixed in this study. In the experimental group, at postoperative 8 weeks, the dome shape of the newly formed bone trabeculae was similar to the curved shape of the SMA device in some specimens. It seems that bone regeneration was induced by the gradual expanding force of the elasticity of the SMA device. Lethaus et al. showed that the newly formed bone in the static periosteal shielding procedure was almost the same as that in the dynamic periosteal elevating procedure.[15] This is different than the present results. They used pig forehead and its skin and soft tissue was much thicker than the rabbit tissue we used. Also, they put every type of devices were put on the same forehead, the tension against the each device may have been less than with the single device used in this study.

The speed of self-activation after removal of the fixation screw seems to be an important factor in acquiring newly formed bone in this method. Sensimen et al. clearly demonstrated that the quality of newly formed bone depended on the distraction speed.[7] Zakaria et al. also reported that the speed of the regenerative space expansion by periosteum elevation should be optimized, and that the speed range of periosteal distraction for bone augmentation was 330 μm per day or less.[9] Measuring the activation speed in this study was difficult, as speed was affected by the form of the device, including the thickness, initial healing around the device, the amount of soft tissue, and body temperature. In addition, only one kind of device was used in this study, so further evaluation is necessary to identify the appropriate form and elasticity of the SMA device.

The role of the mesh-perforations is still a matter of debate. In the previous reports, most of the devices for the periosteal DO or dynamic elevation technique had mesh perforations in the part involved in the traction of the periosteum without standardization of their number or size.[5,7,9] Gosain et al. demonstrated the influence of the periosteal layer on calvarian defects in rabbits.[16] He created a barrier with nonperforated polytetrafluoroethylene membranes that reduced new bone formation in the center of calvarian defects, but simultaneously enhanced bone growth at the peripheral cranial border. Weng et al. demonstrated increased bone growth using the same membranes to shield

the elevated spaces from the periosteum in guided bone regeneration.[17] In the dynamic separating procedure, such as this technique or periosteal distraction, it seems to be important to have sufficient communication between the periosteum and the underside of the device with appropriate mechanical strength against the overlying soft tissue to encourage new bone formation.

Another issue is that nickel may have toxic effects *in vitro* and *in vivo* at high concentrations. The high nickel content of Ni-Ti might cause biocompatibility problems, due to dissolution of nickel ions or wear particles from the alloy.[18] Thus, long-term application of the Ni-Ti alloy should be avoided, and development of a new device with different materials but with the same properties is expected. Few reports have demonstrated ossification between the bone surface and periosteal tissue created by the SMA device after a latency period based on a distraction concept. Macroscopic and microscopic observations conducted in this study revealed no pathological change around the SMA device. Nonetheless this nickel toxicity problem has to be addressed before human use. Recently, new Ni-free, Ti- based alloy was examined for application in orthodontic treatment and craniofacial plastic surgery.[19,20] This material may be suitable for human use.

In medical applications, the mechanical properties and degree of elasticity differ in each treatment. Furthermore the amount of defect is also different especially for the patient who needs a sufficient alveolar bone volume for dental implant. In this study, only one device was used with one protocol, and the number of rabbit was limited according to the Institutional Animal Care and Use Review Committee of the College. So the statistical analysis seems not to be strong enough to prove the ideal protocol for this technique. The results might have been different if we had used other devices with different elasticity or set a longer/shorter latency or consolidation period. SMA materials have been used for bone regeneration or lengthening of the jaw bone.[10,21,22] However, the material was used in the form of a wire, and there is no previous report of using a mesh or board SMA device for a periosteal DO technique.

To the best of our knowledge, this is the first report of newly formed bone in the gap created by the self-activated force using a SMA mesh device. Further studies are needed to provide more information about the newly formed bone and for subsequent use in clinical situations. Improvement in device design and mechanical properties will enable three-dimensional control in craniomaxillofacial surgery and orthopedic surgery. The use of self-activated devices for the periosteal expansion technique may make it possible to avoid the donor site morbidity associated with autogenous tissue grafts, trans-skin, or trans-mucosal activation rods, any bone-cutting procedure, and the following intermittent activation procedure of normal DO.

REFERENCES

1. Sethi A, Kaus T. Ridge augmentation using mandibular block bone grafts: Preliminary results of an ongoing prospective study. Int J Oral Maxillofac Implants 2001;16:378–388.

2. Triplett RG, Schow SR. Autologous bone grafts and endosseous implants: Complementary techniques. J Oral Maxillofac Surg 1996;54:486–494.
3. Chin M, Toth BA. Distraction osteogenesis in maxillofacial surgery using internal devices: Review of five cases. J Oral Maxillofac Surg 1996;54:45–53; discussion 54.
4. Takahashi T, Funaki K, Shintani H, Haruoka T. Use of horizontal alveolar distraction osteogenesis for implant placement in a narrow alveolar ridge: A case report. Int J Oral Maxillofac Implants 2004;19:291–294.
5. Kessler P, Bumiller L, Schlegel A, Birkholz T, Neukam FW, Wiltfang J. Dynamic periosteal elevation. Br J Oral Maxillofac Surg 2007;45:284–287.
6. Oda T, Kinoshita K, Ueda M. Effects of cortical bone perforation on periosteal distraction: An experimental study in the rabbit mandible. J Oral Maxillofac Surg 2009;67:1478–1485.
7. Sencimen M, Aydintug YS, Ortakoglu K, Karslioglu Y, Gunhan O, Gunaydin Y. Histomorphometrical analysis of new bone obtained by distraction osteogenesis and osteogenesis by periosteal distraction in rabbits. Int J Oral Maxillofac Surg 2007;36:235–242.
8. Yamauchi K, Takahashi T, Funaki K, Yamashita Y. Periosteal expansion osteogenesis using highly purified beta-tricalcium phosphate blocks: A pilot study in dogs. J Periodontol 2008;79:999–1005.
9. Zakaria O, Kon K, Kasugai S. Evaluation of a biodegradable novel periosteal distractor. J Biomed Mater Res B Appl Biomater 2012;100:882–889.
10. Goldwaser BR, Papadaki ME, Kaban LB, Troulis MJ. Automated continuous mandibular distraction osteogenesis: Review of the literature. J Oral Maxillofac Surg 2012;70:407–416.
11. Ahlhelm F, Kaufmann R, Ahlhelm D, Ong MF, Roth C, Reith W. Carotid artery stenting using a novel self-expanding braided nickel-titanium stent: Feasibility and safety porcine trial. Cardiovasc Intervent Radiol 2009;32:1019–1027.
12. Liu SS, Kyung HM, Buschang PH. Continuous forces are more effective than intermittent forces in expanding sutures. Eur J Orthodont 2010;32:371–380.

13. Delloye C, Delefortrie G, Coutelier L, Vincent A. Bone regenerate formation in cortical bone during distraction lengthening. An experimental study. Clin Orthop Relat Res 1990;250:34–42.
14. Hikiji H, Takato T, Matsumoto S, Mori Y. Experimental study of reconstruction of the temporomandibular joint using a bone transport technique. J Oral Maxillofac Surg 2000;58:1270–1276; discussion 1277.
15. Lethaus B, Tudor C, Bumiller L, Birkholz T, Wiltfang J, Kessler P. Guided bone regeneration: Dynamic procedures versus static shielding in an animal model. J Biomed Mater Res B Appl Biomater 2010;95:126–130.
16. Gosain AK, Santoro TD, Song LS, Capel CC, Sudhakar PV, Matloub HS. Osteogenesis in calvarial defects: Contribution of the dura, the pericranium, and the surrounding bone in adult versus infant animals. Plast Reconstr Surg 2003;112:515–527.
17. Weng D, Hürzeler MB, Quiñones CR, Ohlms A, Caffesse RG. Contribution of the periosteum to bone formation in guided bone regeneration. A study in monkeys. Clinical Oral Implants Res 2000;11:546–554.
18. Kapanen A, Ryhänen J, Danilov A, Tuukkanen J. Effect of nickel-titanium shape memory metal alloy on bone formation. Biomaterials 2001;22:2475–2480.
19. Kanetaka H, Shimizu Y, Kudo TA, Zhang Y, Kano M, Sano Y, Ichikawa H, Hosoda H, Miyazaki S. New internalized distraction device for craniofacial plastic surgery using Ni-free, Ti-based shape memory alloy. J Craniofac Surg 2010;21:1839–1842.
20. Suzuki A, Kanetaka H, Shimizu Y, Tomizuka R, Hosoda H, Miyazaki S, Okuno O, Igarashi K, Mitani H. Orthodontic buccal tooth movement by nickel-free titanium-based shape memory and superelastic alloy wire. Angle Orthod 2006;76:1041–1046.
21. Idelsohn S, Peña J, Lacroix D, Planell JA, Gil FJ, Arcas A. Continuous mandibular distraction osteogenesis using superelastic shape memory alloy (SMA). J Mater Sci Mater Med 2004;15:541–546.
22. Xie M, Hu M, Liu H, Xiao H. Primary study of the use of an internal, self-activated shape memory alloy distraction device in the dog mandible: Alveolar ridge distraction and implant placement. J Oral Maxillofac Surg 2011;69:2033–2039.

Reconstitution of Human *Ether-a-go-go*-Related Gene Channels in Microfabricated Silicon Chips

Azusa Oshima,[†] Ayumi Hirano-Iwata,[*,†,‡] Hideki Mozumi,[†] Yutaka Ishinari,[†] Yasuo Kimura,[§] and Michio Niwano[†,§]

[†]Graduate School of Biomedical Engineering, Tohoku University, 6-6 Aoba, Aramaki, Aoba-ku, Sendai 980-8579, Japan

[‡]PRESTO, Japan Science and Technology Agency (JST), 4-1-8 Honcho Kawaguchi, Saitama 332-0012, Japan

[§]Laboratory for Nanoelectronics and Spintronics, Research Institute of Electrical Communication, Tohoku University, 2-1-1 Katahira, Aoba-ku, Sendai, Miyagi 980-8577, Japan

🅢 Supporting Information

ABSTRACT: This paper reports on the reconstitution of human *ether-a-go-go*-related gene (hERG) channels in artificial bilayer lipid membranes (BLMs) formed in micropores fabricated in silicon chips. The hERG channels were isolated from Chinese hamster ovary cell lines expressing the channels and incorporated into the BLMs formed by a process in which the two lipid monolayers were folded into the micropores. The characteristic features of hERG channels reported by the patch-clamp method, including single-channel conductance, voltage dependence, sensitivity to typical drugs and dependence on the potassium concentration, were investigated in the BLM reconstitution system. The BLM with hERG channels incorporated exhibited a lifetime of ~65 h and a tolerance to repetitive solution exchanges. Such stable BLMs containing biological channels have the potential for use in a variety of applications, including high-throughput drug screening for various ion-channel proteins.
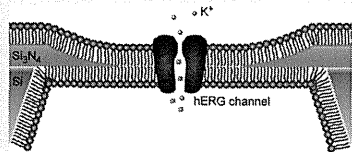
I on-channel proteins are membrane proteins that are of crucial physiological importance and are major targets for drug design.[1,2] Recording ion-channel activities by measuring ion currents represents a simple method to investigate channel function[3] and to screen the effect of drug candidates.[4] Much of our understanding of ion-channel proteins has arisen from data obtained using the patch-clamp method for recording ion flux through open channels at the single-channel and whole-cell levels. On the other hand, the reconstitution of ion channels in artificial bilayer lipid membranes (BLMs) has the advantage that the researcher can precisely control the composition of the system, including the lipid environment, which is not easily manipulated in the case of the patch-clamp method. However, the mechanical instability of BLMs prevents them from being widely used and, as a result, the bilayer method in currently confined to laboratory use.

There is a growing interest in the development of drug screening platforms for ion channels, since a wide range of ion channels has been identified, not only as a primary molecular target in drug actions but also as a major culprit in drug-induced adverse effects.[4] A recent example that received considerable attention is the human *ether-a-go-go*-related gene (hERG) channel,[5] a cardiac voltage-dependent potassium channel. Full or partial blockage of the hERG channel by drugs that are designed for totally unrelated targets can result in a potentially fatal arrhythmia.[6,7] A number of drugs, including antihistamines, antipsychotics, gastric prokinetics, and even antibiotics, have now been withdrawn from the market because of their adverse effects on the hERG channel.[6] In accordance

with the ICH S7B safety guideline,[8] regulatory agencies require that the potential for drug candidates to inhibit cardiac ion-channels be assessed, particularly hERG, before clinical trials are performed.[4,6,9] Although the guideline mentions cell-based electrophysiological assays as an in vitro assessment method, it also states that novel channel activity assays could be useful in the preliminary screening of test substances. BLM, in which the hERG channel is incorporated, represents a potentially new technique for screening substances that directly block hERG channels, provided issue of membrane instability is addressed and solved.

Numerous attempts have been made to improve the stability of BLMs through the formation of BLMs in nano- and microfabricated pores.[10–17] These efforts led to the prolongation of membrane lifetime of several tens of hours.[12,18] However, the mechanical stability of BLMs has not been improved to the desired extent. In addition, these approaches are commonly based on BLMs prepared from lipids dissolved in n-alkane solvents, which are probably not found in naturally occurring cell membranes. Since residual solvent may be present in the annular region and/or in the bilayer interior, as indicated by capacitance measurements,[19,20] and the partitioning of n-alkanes into BLMs has been reported to decrease with n-alkane chain length,[21] the use of large amounts of the solvent,

especially shorter chained n-alkanes, may denature the fragile ion-channel proteins. For the above reasons, it would be highly desirable to minimize n-alkane solvent levels in BLMs as a new drug screening platform for ion channels, although solvents may contribute to the formation of stable BLMs.[22]

The use of an n-alkane solvent has been a common approach for improving BLM stability.[11–15,23–26] The solvents increase hydrophobicity of the pore rim and permit the lipids near the edge of the pore to become oriented appropriately.[22] In addition, a nonpolar solvent may function as an insulator to prevent electric leakage in the membrane edge area.[22] In another approach to the formation of stable BLMs, we reported on the formation of mechanically stable and reduced-solvent BLMs by preparing membranes in microfabricated pores, the edges of which were smoothly tapered.[27] The pores were fabricated in a nanometer-thick silicon nitride (Si₃N₄) septum deposited on a Si substrate. The BLMs formed in the pore showed tolerance to a high applied voltage (±1 V) and mechanical shock during repetitive solution exchanges, together with a long lifetime over 40 h. The key feature that stabilized the BLMs is probably the tapered shape of the pore edge that was formed via isotropic etching. This shape allows stress on the bilayer to be reduced at the point of contact with the septum, leading to the formation of stable BLMs. At first, the BLMs formed in the pores of these Si chips exhibited a large background noise and slow current transients for open ↔ close events, due to the large capacitance of the Si chip. To eliminate this, we reduced the chip capacitance by coating the chip with layers of insulation.[28] After coating the chip, except for the pore, with Teflon and SiO₂, the noise level and current transients were improved without any detectable impairment in membrane stability.

In the present study, we used this stable BLM to measure the ion current of the hERG channel, which is highly important as a target of the early toxicity screening of preclinical drug candidates.[4,6–9] The hERG channels (Kv11.1) were isolated from Chinese hamster ovary (CHO) cell lines expressing the channels and were incorporated into the BLMs suspended in the micropores that were fabricated in the Si Chips. Ion currents of single or multiple hERG channels were investigated in terms of single-channel conductance, voltage dependence, sensitivity to typical drugs and potassium concentration dependence.

◼ EXPERIMENTAL SECTION

Materials. CHO cell lines expressing hERG channels (Kv11.1) were obtained from the Channelopathy Foundation (Basel, Switzerland). Chloroform solutions of L-α-phosphatidylcholine, (PC, from egg) and L-α-phosphatidylethanolamine [PE, transphosphatidylated (egg)] were purchased from Avanti Polar Lipids (Alabaster, AL). Cholesterol (Chol) was obtained from Wako Pure Chemicals (Osaka, Japan) and recrystallized three times from methanol. E-4031 and astemizole were obtained from Wako Pure Chemicals and Sigma-Aldrich (St. Louis, MO), respectively. FZ Si (100) wafers (>9000 Ω cm, 200 μm in thickness), one side of which was coated with a 240 nm thick Si₃N₄ layer, were obtained from Semitec (Chiba, Japan). Teflon-AF (type 1601, 6% solution in Fluorinert FC-40) was purchased from DuPont Fluoroproducts (Wilmington, DE). 3-Cyanopropyldimethylchlorosilane (CPDS) was obtained from Gelest (Morrisville, PA). Acetonitrile for HPLC was purchased from Wako Pure Chemicals.

Protein Isolation. The hERG channels were extracted from CHO cell lines as membrane fractions, according to the procedures in ref 29. Briefly, the cells obtained from 100 mm plates were rinsed with HBSS (GIBCO) and scraped off into a 3 mL solution of 200 mM NaCl, 33 mM NaF, 10 mM EDTA, and 50 mM HEPES (pH 7.4 with NaOH) plus protease inhibitors (100 μM phenylmethylsulfonyl fluoride, 1 μg/mL pepstatin A, 1 μg/mL leupeptin). The cells were homogenized and spun at 1500g for 10 min. The membrane fractions were pelleted from the low-speed supernatants by centrifugation at 157000g for 1 h and resuspended in 120 mM KCl and 10 mM HEPES (pH 7.2 KOH). All steps were performed at 4 °C. The total protein concentration in the protein suspension was determined by the Bradford method using a BIO-RAD protein assay kit. The total protein concentration ranged from 1.3 to 1.9 mg/mL (total volume of 0.5–0.6 mL) among 5 isolation experiments. Since the protein was obtained in the form of a crude membrane preparation, the protein samples produced various bands on an SDS–PAGE gel, including a band at ~155 kDa corresponding to hERG[29,30] (Figure S2 of the Supporting Information).

BLM Formation. Micropores with a diameter of 20–60 μm were fabricated in Si chips, and the surface of the chip was coated with Teflon-AF and thermal oxide, according to the procedure described in ref 28. The Si chip thus fabricated was silanized by treating with 2% (v/v) CPDS in acetonitrile from 1– 2 h at room temperature in a nitrogen-filled glovebox. Planar BLMs were formed by folding up two lipid monolayers across the micropore in the Si chip, which was set in the middle of a Teflon chamber (Figure 1). The Si chip separated two
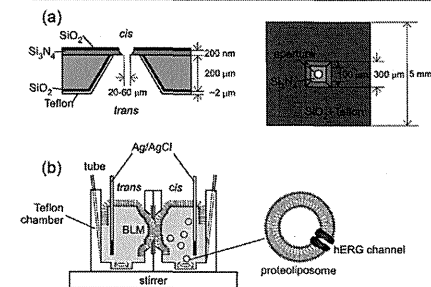
Figure 1. (a) Cross-section and top view of a silicon chip suspending BLMs (not drawn to scale). (b) Schematic of a BLM formed across a micropore in the present Si chip.

compartments, cis and trans, in the chamber. Each side of the chip was precoated with a thin layer of n-hexadecane, by applying a 5 μL aliquot of 0.1% n-hexadecane in chloroform. Although solvent-free BLMs were also formed without n-hexadecane precoating in the Si chip,[27] this primer coating appeared to improve the probability of stable BLM formation. A 1350 μL portion of 22 mM KCl solution containing 10 mM HEPES/KOH (pH 7.2) (abbreviated as 22 mM KCl buffer), filtered just before use through a cellulose acetate filter (pore size 0.20 μm; Advantec Toyo), was added to each compartment of the chamber. The buffer level in both compartments was set below the pore. A 10 μL portion of a lipid solution [2 mg/mL

ACS Publications © 2013 American Chemical Society   4363   dx.doi.org/10.1021/ac303484k | Anal. Chem. 2013, 85, 4363–4369

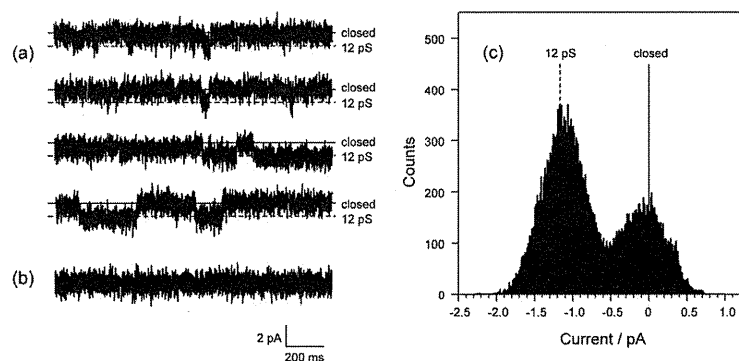4364   dx.doi.org/10.1021/ac303484k | Anal. Chem. 2013, 85, 4363–4369

262

Figure 2. Single hERG channel currents recorded at an applied potential of −100 mV. (a) Before the addition of E-4031 (control). (b) After the addition of E-4031. The final concentration of E-4031 was 200 μM. (c) Point-amplitude histogram of the current trace shown in (a).
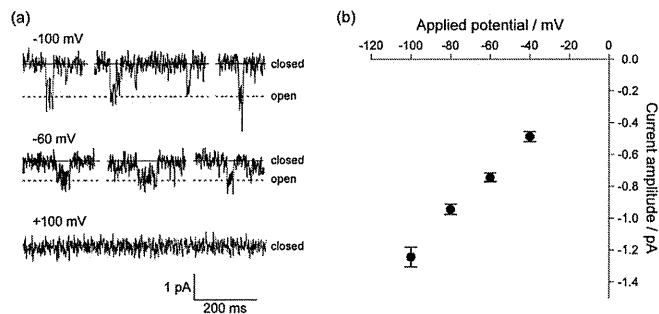

Figure 3. (a) Examples of single hERG channel currents recorded at an applied potential of −100, −60, and +100 mV. (b) Single-channel current–voltage (I–V) relationship for hERG. The error bar indicates the SEM (n = 3–7).

PC:PE:Chol = 7:1:2 (w/w) in chloroform/n-hexane (1:1, v/v)] was spread on the aqueous solutions. After evaporation of the chloroform/n-hexane, the BLMs were formed by gradually raising the buffer level until it surpassed the pore.

Protein Incorporation and Current Recordings. The incorporation of hERG channels into planar BLMs was performed by fusing hERG-containing proteoliposomes either with the preformed BLMs or with the lipid monolayer on the cis solution before BLM formation. In the former method, a proteoliposome suspension (typically 100 μL) containing hERG channels was added to the cis solution after the formation of the BLMs. A 50 μL aliquot of a 3.0 M KCl solution containing 10 mM HEPES/KOH (pH 7.2) (abbreviated as 3.0 M KCl buffer) was added to the cis side to adjust the KCl concentration to 120 mM to generate a potassium concentration gradient across the BLMs. After gentle stirring for 30–60 min, a 50 μL aliquot of the 3.0 M KCl buffer was added to the trans side. In the latter method, lipid monolayers were first spread on the solutions in both cis and trans compartments. After evaporation of the solvent, a protein suspension (typically 100 μL) containing hERG channels was

added to the cis solution. The buffer level in both compartments was then gradually raised to allow the monolayer containing the hERG channels (cis side) and that containing only lipids (trans side) to undergo folding. In both methods, the cis and trans compartments were finally filled with a solution containing 120 mM KCl and 10 mM HEPES/KOH (pH 7.2) (abbreviated as 120 mM KCl buffer). Sometimes the incorporation processes in both cases were performed in a hot water bath (70–80 °C), which made the temperature of the cis and trans solutions about 37 °C. The use of physiological temperature was based on our previous observation that the rate of incorporation of a gramicidin channel into BLMs was improved when the temperature of the aqueous solutions surrounding BLMs was warmed to ~37 °C.[28] The success probability for observing hERG channel currents for 53 membranes was 13%. Channel blockers (E-4031 and astemizole) were added to both sides of the BLMs in order to avoid changes in the concentration of astemizole, which is highly hydrophobic and membrane permeant.[31]

Current recordings and capacitance measurements were performed with an Axopatch 200B patch-clamp amplifier

---

(Molecular Devices). Signals were online filtered at 1 kHz with a low-pass Bessel filter, digitized at 10 kHz, and stored online using a data acquisition system (Digidata 1440 and pCLAMP 10.2, Molecular Devices). The currents were off-line filtered at a cutoff frequency of 0.7 kHz, according to a literature describing patch-clamp recordings of single hERG currents.[32] Applied potentials were defined with respect to the trans side held at ground. Capacitance was measured by applying ramp voltage pulses of 4 V/s at a holding potential of 0 mV. The total capacitance (the sum of both membrane and device capacitance) was 39 ± 12 pF (n = 8) in 22 mM KCl buffer and 46 ± 7.9 pF (n = 3) in 120 mM KCl buffer. Average currents for multichannel responses during open periods were obtained as described in the Supporting Information.

■ RESULTS AND DISCUSSION

hERG Single-Channel Currents. The hERG channel is a voltage-gated potassium channel that is crucial for repolarization during action potentials in human ventricular myocytes.[7,33] We first examined recordings of the hERG single-channel currents (Figure 2) after incorporation of the hERG channel into BLMs formed in the microfabricated Si chip. Stepwise currents were evident, with an average single-channel chord conductance of 11 ± 1.2 pS (mean ± SEM, n = 3). This conductance level is similar to a previously reported value (12 pS in 120 mM KCl) obtained using the patch-clamp method.[32] The addition of E-4031, a specific blocker,[34,35] completely blocked channel activity, confirming the functionality of the hERG channel incorporated in the BLMs formed in the Si chips. Single-channel activity was only observed at negative applied potentials, as shown in the I–V relationship of single hERG currents (Figure 3). The slope conductance for the inward currents, determined by linear regression analysis of the I–V relationship between −100 and −40 mV, was also 12 pS. At positive potentials, no outward currents were observed, which is in agreement with reported patch-clamp observations showing that outward single-channel currents are only infrequently observed for hERG channels expressed in Xenopus oocytes.[32] Artificial BLMs formed in microfabricated Si chips have been criticized from the standpoint that the BLMs exhibit a high background noise level due to the large device capacitance in the range from 250 pF to 1 nF.[12,14,27,36] However, after the Si chip was coated with capacitance-reducing insulating layers (Teflon and thermal oxide),[28] the total capacitance (the sum of both membrane and device capacitance) was reduced to 46 ± 7.9 pF (n = 3) in 120 mM KCl buffer. The BLMs formed in this chip showed an rms noise of 1.5 ± 0.40 pA in a 5 kHz bandwidth and the peak-to-peak noise of 1−2 pA after filtering at 1 kHz. The use of a SiO$_2$/Teflon dielectric layer greatly reduces the noise level, which permitted single-channel activities of the hERG channel, whose conductance is relatively low, to be recorded.

hERG Multi-Channel Currents and Protein Orientation. In addition to stepwise single-channel currents, large and intermittent burstlike currents were observed in some membranes (Figure 4), indicating the presence of multiple channels in the BLM. The current corresponds to the sum of the ion flow through the open channels whose number fluctuates from moment to moment. The number of open hERG channels, as estimated based on the single-channel current (~1 pA at −100 mV), varied from zero to more than ten. Since the number of hERG channels in the BLM is still fairly small, their open ↔ close transitions are stochastic. To

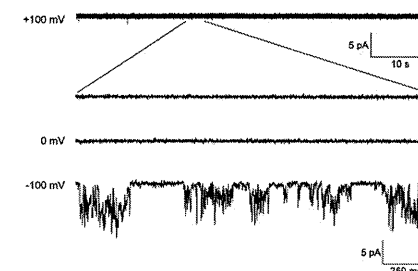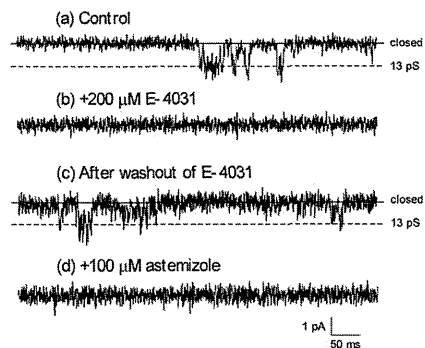Figure 4. hERG multichannel currents recorded at an applied potential of +100, 0, and −100 mV.

examine the variation in the currents, we repeated multichannel recordings with a single BLM, and the average current during the open period was estimated (see the Supporting Information). The relative standard deviation obtained for four sets of ~10 s open durations was 40%. Because the number of open hERG channels fluctuates in a stochastic manner, relatively large variations were observed for the multichannel currents. Interestingly, burstlike multichannel currents were observed only at −100 mV, while no current fluctuations were observed at +100 mV. This means that most of the hERG channels were embedded in the BLM with the intracellular side oriented toward the cis side. Of the seven BLMs that showed hERG channel activities, including multi- and single-channel currents, five (71%) showed channel activity only at negative potentials, suggesting that the incorporation of a hERG channel proceeds preferentially in an orientation such that the cis side chamber corresponds to the cytoplasmic space and the trans to the extracellular space. Since the hERG-containing proteoliposomes were prepared from a crude membrane fraction without a detergent-solubilization process, there may be preferential channel orientation in liposomes, leading to the oriented reconstitution of hERG channels in the BLMs. A similar oriented reconstitution in BLMs has been reported for ion channels isolated without detergent purification (e.g., calcium-activated K⁺ channels from rat myometrium vesicles[37] and voltage-dependent Cl⁻ channels from rabbit skeletal muscle).[38]

Effect of Drugs on hERG Channel Currents. The hERG channel is the most important component of phase 3 repolarization during the action potential in human ventricular myocytes.[7,33] The full or partial blockage of the hERG channel causes a long QT syndrome, a cardiac repolarization disorder that predisposes people to cardiac arrhythmia.[6,7] Various drugs, including antihistamines and antibiotics, can block hERG channels and trigger ventricular arrhythmia and, in some cases, result in sudden death.[6,7] It therefore becomes highly important to analyze the effects of a drug on hERG single-channel activity via the use of BLM reconstitution systems, where hERG channel activities can be evaluated under chemically controlled conditions.

Figure 5 shows the effects of E-4031 and astemizole on hERG currents at the single-channel level. E-4031 is a specific channel blocker of hERG, and astemizole is an antihistamine that has been withdrawn from the market in most countries due to its side effect on the hERG channel.[4,7] Before the addition of

263

(a) Control

closed

13 pS

(b) +200 µM E- 4031

(c) After washout of E- 4031
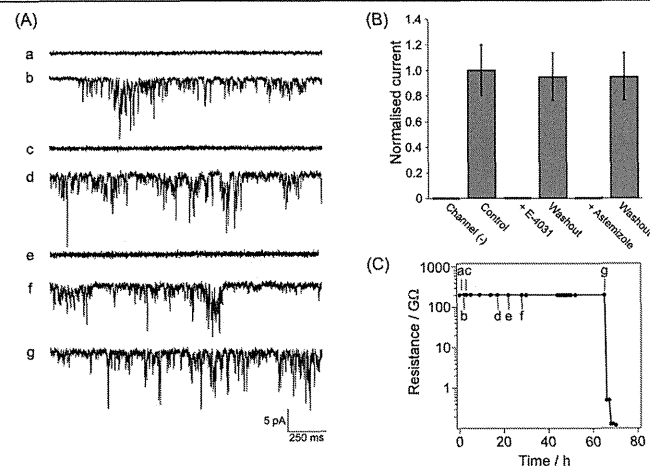
closed

13 pS

(d) +100 µM astemizole

1 pA

50 ms

Figure 5. Blocking of a single hERG channel by E-4031 and astemizole. (a) Before the addition of blockers (control). (b) After the addition of E-4031. The final concentration of E-4031 was 200 µM. (c) Recovery from E-4031 block after thorough washout. (d) After the addition of astemizole. Final concentration of astemizole was 100 µM. Applied potential: −100 mV.
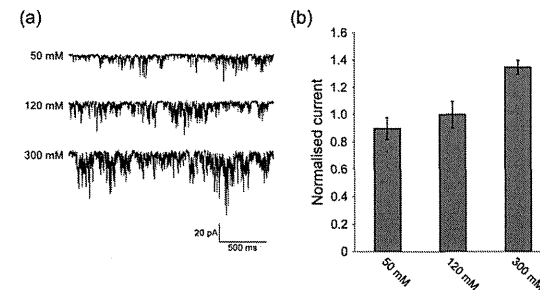
the drugs (control), stepwise currents were observed with a single-channel conductance of ~13 pS. The addition of E-4031 completely blocked the current, thus confirming that the control currents stemmed from the permeation of ions through the hERG channel. After washing out E-4031, the channel activities were recovered. Finally, the addition of astemizole again completely blocked the channel current, confirming its inhibitory effect on hERG channels reconstituted in a BLM. Thus, the sensitivity of the hERG channel to most typical drugs has been successfully reproduced in the present BLM reconstitution system. For a detailed analysis of the blocked states of hERG at lower drug concentrations, a faster sampling rate with a higher cutoff frequency would be necessary to increase time resolution because blockers can reduce the open state of ion channels.[39] As shown in Figures 3a and 5, the open channel noise was sometimes higher than the closed-state noise, probably because the opening dynamics of the hERG channels is faster than the resolution of detection, even in the absence of blockers. A higher current noise at the open state than the closed state was also reported for hERG channels in Xenopus oocytes.[32] An enhanced time resolution will likely be required to resolve the intermediate states of channels at low drug concentrations. However, a lower noise level is a prerequisite for achieving a higher sampling rate, leading to a higher temporal resolution.

Multiple hERG channels are sometimes integrated in BLM as observed in Figure 6. hERG channel activities were observed only after the incorporation of channels into BLMs and were blocked completely by the addition of E-4031. After a thorough washout of E-4031 for ~17 h, channel activities were fully recovered. The further addition of astemizole also blocked the activity of the hERG channel, again reproducing the adverse effect of astemizole on hERG channels in the BLM system. The

(A)

a

b

c

d

e

f

g

5 pA

250 ms

(B)

Normalised current

1.4
1.2
1.0
0.8
0.6
0.4
0.2
0

Channel (-)   Control   + E-4031   Washout   + Astemizole   Washout

(C)

Resistance / GΩ

1000
100
10
1

0   20   40   60   80

Time / h

Figure 6. Blocking of hERG channels by E-4031 and astemizole at the multichannel level. (A) Examples of hERG multichannel currents recorded at an applied potential of −100 mV. (a) Before the incorporation of hERG into the BLM. (b) Control hERG multichannel current before addition of blockers. (c) After the addition of E-4031. The final concentration of E-4031 was 200 µM. (d) Recovery from E-4031 blocking after a thorough washout. (e) After the addition of astemizole. The final concentration of astemizole was 100 µM. (f) Recovery from astemizole blocking after a thorough washout. (g) hERG channel currents ~65 h after BLM formation. (B) Channel-current amplitude normalized to the control (trace b in A). Average current amplitude was first calculated as described in the Supporting Information and normalized to the control value. The error bar indicates the SEM (n = 4–5). (C) Time-course of the resistance obtained from the BLM from which the current traces in (A) were recorded. Points a–g represent points at which the current traces a–g in (A) were recorded.

(a)

50 mM

120 mM

300 mM

20 pA

500 ms

(b)

Normalised current

1.6
1.4
1.2
1.0
0.8
0.6
0.4
0.2
0

50 mM   120 mM   300 mM

Figure 7. Potassium concentration dependence on hERG multichannel currents. (a) Examples of hERG multichannel currents at 50, 120, and 300 mM K⁺. Applied potential: −200 mV. (b) Normalized-current amplitude at 50, 120, and 300 mM K⁺. Current amplitude was normalized to that obtained in 120 mM KCl. The error bar indicates the SEM (n = 12–30).

blocking by astemizole was reversed after a washout of several hours. The channel activities were still observed even after ~65 h, demonstrating that present BLM in the micropores is stable and retains high-sealing properties for long hours. Although both E-4031 and astemizole blocked the hERG channel, the recovery from the E-4031 blocking was much slower than for the blocking by astemizole (Figure S3 of the Supporting Information), suggesting that the blocking by the two compounds is controlled by two different mechanisms.[31,40,41] A similar recovery from the drug-induced blocking has been reported by the patch-clamp method; hERG currents recover from E-4031 blocking extremely slowly, requiring more than 1 h,[42] while faster recovery has been reported for astemizole blocking.[31] Furthermore, a full recovery from the E-4031 blocking was also achieved in the present system after repeating the washout process for a long period, owing to the high mechanical stability. The BLM-containing hERG channels withstood repetitive (17 times) exchanges of solutions during the ~65 h measurements. These results demonstrate that the present BLM has the potential for being particularly useful for examining the long-term effect of drugs on hERG channels. The importance and difficulty in exchanging solutions adjacent to BLMs was also pointed out by Portonovo and Schmidt.[43] Solution exchange enables different experimental conditions for the same BLM preparation. In our experiments most BLM preparations with integrated ion channels (hERG or other channels) withstood solution exchanges (92%, 13 BLMs were examined). Such a high compatibility of the BLMs to solution exchanges can be useful for increasing the experimental throughput from single BLMs.

Finally, we examined the potassium concentration dependence on hERG multichannel currents (Figure 7). It has been reported that the conductance of hERG is dependent on the potassium concentration and is saturated at high concentrations.[44] When the concentration of potassium was reduced to 50 mM, the multichannel response was reduced to ~90%, while, when the potassium concentration was increased to 300 mM, the multichannel response was also increased to ~130%. The observed potassium concentration dependence was similar to that reported for hERG channels investigated using the patch-clamp method.[44] Therefore, the hERG channels incorporated into the present BLM system showed a similar sensitivity to potassium concentration to that reported for

hERG channels in cell membranes. On the basis of the above results, it can be concluded that the hERG channels incorporated in the present BLMs retain their characteristic pharmacological sensitivities to typical blockers as well as to the concentration of potassium, demonstrating intact reconstitution of hERG channels in the Si chip-based BLM systems.

■ CONCLUSIONS

We report herein on the incorporation of intact hERG channels into artificial BLMs suspended in microfabricated Si chips. The BLMs with integrated hERG channels are highly stable for long periods. The characteristic features of hERG channels, such as single-channel conductance, voltage dependence, sensitivity to typical drugs and potassium concentration dependence, were retained after being incorporated into the BLM in Si chips. These results demonstrate the significant potential of the present hERG-based Si chip as a platform for drug safety screens. It could also be used to evaluate long-term or hysteresis effects of drugs, as the present BLM containing hERG channels exhibited a long lifetime (~65 h) together with mechanical stability to repetitive solution exchanges. Since the number of hERG channels in the BLM is fairly small, and the observed single- and multichannel events are stochastic, investigations of dose-dependent inhibition are not as easy as in the case of whole-cell current measurements. However, the analysis of single-channel currents sheds considerable information on the mechanism of drug-induced inhibition than whole-cell measurements: the issue of whether a drug of interest causes a reduction in single-channel conductance or a reduction in open time could be a useful measure for investigating the inhibition mechanism and designing new drugs without side effects. Although we used identical potassium ion concentrations on both sides of BLMs to compare the results with reported single-channel properties measured in cell-attached patches, the present approach is generally applicable to other experimental conditions, including asymmetric solution conditions.

The next step is to extend the stable hERG-containing BLM device to a multisite array format for use as a platform for hERG safety screens. Since we previously reported on the simultaneous and automated formation of stable BLMs in a horizontal array format and parallel recordings of channel activities from different BLMs,[45] in future studies, we plan to

improve the throughput by combining the hERG-containing BLMs with the array format. We conclude that the realization of a hERG-channel array will open a variety of applications, including high-throughput drug screening procedures that can be a complement to the patch-clamp method.

■ ASSOCIATED CONTENT

● Supporting Information

Additional description on the analysis of multichannel currents, SDS–PAGE of crude membrane extracts from CHO cells expressing hERG channels, and time courses for the fraction of open durations during drug-induced channel inhibition and recovery from blocking. This material is available free of charge via the Internet at http://pubs.acs.org.

■ AUTHOR INFORMATION

Corresponding Author
*E-mail: ahirano@bme.tohoku.ac.jp. Tel: +81-22-795-4866. Fax: +81-22-795-4863.

Notes
The authors declare no competing financial interest.

■ ACKNOWLEDGMENTS

■ REFERENCES

(1) Overington, J. P.; Al-Lazikani, B.; Hopkins, A. L. *Nat. Rev. Drug Discovery* 2006, *5*, 993–996.

(2) Ashcroft, F. M. *Nature* 2006, *440*, 440–447.

(3) Miller, C. *Ion Channel Reconstitution*; Plenum Press: New York, 1986.

(4) Dunlop, J.; Bowlby, M.; Peri, R.; Vasilyev, D.; Arias, R. *Nat. Rev. Drug Discovery* 2008, *7*, 358–368.

(5) Vandenberg, J. I.; Perry, M. D.; Perrin, M. J.; Mann, S. A.; Ke, Y.; Hill, A. P. *Physiol. Rev.* 2012, *92*, 1393–1478.

(6) Neubert, H.-J. *Anal. Chem.* 2004, *76*, 327 a–330a.

(7) Sanguinetti, M. C.; Tristani-Firouzi, M. *Nature* 2006, *44*, 463–469.

(8) International Conference on Harmonisation of Technical Requirements for Registration of Pharmaceuticals for Human Use (ICH). *ICH Harmonised Tripartite Guideline: The Non-Clinical Evaluation of the Potential for Delayed Ventricular Repolarization (QT Interval Prolongation) By Human Pharmaceuticals S7B*, current Step 4 version; ICH: Geneva, 2005 (http://www.ich.org/products/guidelines/safety/article/safety-guidelines.html).

(9) Gintant, G. *Pharmacol. Ther.* 2011, *129*, 109–119.

(10) Schmidt, C.; Mayer, M.; Vogel, H. *Angew. Chem., Int. Ed.* 2000, *39*, 3137–3140.

(11) Römer, W.; Steinem, C. *Biophys. J.* 2004, *86*, 955–965.

(12) Han, X. J.; Studer, A.; Sehr, H.; Geissbühler, I.; Di Berardino, M.; Winkler, F. K.; Tiefenauer, L. X. *Adv. Mater.* 2007, *19*, 4466–4470.

(13) Schibel, A. E. P.; Edwards, T.; Kawano, R.; Lan, W.; White, H. S. *Anal. Chem.* 2010, *82*, 7259–7266.

(14) Wilk, S. J.; Petrossian, L.; Goryll, M.; Thornton, T. J.; Goodnick, S. M.; Tang, J. M.; Eisenberg, R. S. *Biosens. Bioelectron.* 2007, *23*, 183–190.

(15) Pioufle, B. L.; Suzuki, H.; Tabata, K. V.; Noji, H.; Takeuchi, S. *Anal. Chem.* 2008, *80*, 328–332.

(16) Sumitomo, K.; Tamba, Y.; Shinozaki, Y.; Torimitsu, K. *Appl. Phys. Express* 2010, *3*, 107001.

(17) Hirano-Iwata, A.; Niwano, M.; Sugawara, M. *Trends Anal. Chem.* 2008, *27*, 512–520.

(18) Liu, B.; Rieck, D.; Van Wie, B. J.; Cheng, G. J.; Moffett, D. F.; Kidwell, D. A. *Biosens. Bioelectron.* 2009, *24*, 1843–1849.

(19) Benz, R.; Fröhlich, O.; Läuger, P.; Montal, M. *Biochim. Biophys. Acta* 1975, *394*, 323–334.

(20) White, S. H. *Biochim. Biophys. Acta* 1974, *356*, 8–16.

(21) Coster, H. G. L.; Laver, D. R. *Biochim. Biophys. Acta* 1986, *857*, 95–104.

(22) Batishchev, O. V.; Indenbom, A. V. *Bioelectrochemistry* 2008, *74*, 22–25.

(23) Leptihn, S.; Thompson, J. R.; Ellory, J. C.; Tucker, S. J.; Wallace, M. I. *J. Am. Chem. Soc.* 2011, *133*, 9370–9375.

(24) Studer, A.; Demarche, S.; Langenegger, D.; Tiefenauer, L. *Biosens. Bioelectron.* 2011, *26*, 1924–1928.

(25) Zagnoni, M.; Sandison, M. E.; Morgan, H. *Biosens. Bioelectron.* 2009, *24*, 1235–1240.

(26) Syeda, R.; Holden, M. A.; Hwang, W. L.; Bayley, H. *J. Am. Chem. Soc.* 2008, *130*, 15543–15548.

(27) Hirano-Iwata, A.; Aoto, K.; Oshima, A.; Taira, T.; Yamaguchi, R. T.; Kimura, Y.; Niwano, M. *Langmuir* 2010, *26*, 1949–1952.

(28) Oshima, A.; Hirano-Iwata, A.; Nasu, T.; Kimura, Y.; Niwano, M. *Micro Nanosyst.* 2012, *4*, 2–7.

(29) Zhou, Z.; Gong, Q.; Ye, B.; Fan, Z.; Makielski, J. C.; Robertson, G. A.; January, C. T. *Biophys. J.* 1998, *74*, 230–241.

(30) Ehrlich, J. R.; Pourrier, M.; Weerapura, M.; Ethier, N.; Marmabachi, A. M.; Hébert, T. E.; Nattel, S. *J. Biol. Chem.* 2004, *279*, 1233–1241.

(31) García-Ferreiro, R. E.; Kerschensteiner, D.; Major, F.; Monje, F.; Stühmer, W.; Pardo, L. A. *J. Gen. Physiol.* 2004, *124*, 301–317.

(32) Zou, A.; Curran, M. E.; Keating, M. T.; Sanguinetti, M. C. *Am. J. Physiol.* 1997, *272*, H1309–H1314.

(33) Hancox, J. C.; McPate, M. J.; El Harchi, A.; Zhang, Y. H. *Pharmacol. Ther.* 2008, *119*, 118–132.

(34) Trudeau, M. C.; Warmke, J. W.; Ganetzky, B.; Robertson, G. A. *Science* 1995, *269*, 92–95.

(35) Liu, G. X.; Zhou, J.; Nattel, S.; Koren, G. *J. Physiol.* 2004, *556*, 401–413.

(36) Maurer, J. A.; White, V. E.; Dougherty, D. A.; Nadeau, J. L. *Biosens. Bioelectron.* 2007, *22*, 2577–2584.

(37) Toro, L.; Ramos-Franco, J.; Stefani, E. *J. Gen. Physiol.* 1990, *96*, 373–394.

(38) Ide, T.; Hidaka, J.; Kasai, M. *Biochim. Biophys. Acta* 1995, *1237*, 115–120.

(39) Colquhoun, D.; Hawkes, A. G. In *Single-Channel Recording*, 2nd ed.; Sakmann, B.; Neher, E., Eds.; Plenem Press: New York, NY, 1995; pp 397–482.

(40) Kamiya, K.; Niwa, R.; Mitcheson, J. S.; Sanguinetti, M. C. *Mol. Pharmacol.* 2006, *69*, 1709–1716.

(41) Stork, D.; Timin, E. N.; Berjukow, S.; Huber, C.; Hohaus, A.; Auer, M.; Hering, S. *Br. J. Pharmacol.* 2007, *151*, 1368–1376.

(42) Ishii, K.; Nagai, M.; Takahashi, M.; Endoh, M. *Cardiovasc. Res.* 2003, *57*, 651–659.

(43) Portonovo, S. A.; Schmidt, J. *Biomed. Microdevices* 2012, *14*, 187–191.

(44) Kiehn, J.; Lacerda, A. E.; Wible, B.; Brown, A. M. *Circulation* 1996, *94*, 2572–2579.

(45) Hirano-Iwata, A.; Nasu, T.; Oshima, A.; Kimura, Y.; Niwano, M. *Appl. Phys. Lett.* 2012, *101*, 023702.

Colloids and Surfaces B: Biointerfaces

Effect of ammonia or nitric acid treatment on surface structure, in vitro apatite formation, and visible-light photocatalytic activity of bioactive titanium metal

CrossMark

Masakazu Kawashita [a,*], Naoko Matsui [a], Toshiki Miyazaki [b], Hiroyasu Kanetaka [c]

[a] Graduate School of Biomedical Engineering, Tohoku University, Sendai 980-8579, Japan
[b] Graduate School of Life Science and Systems Engineering, Kyushu Institute of Technology, Kitakyushu 808-0196, Japan
[c] Liaison Center for Innovative Dentistry, Graduate School of Dentistry, Tohoku University, Sendai 980-8575, Japan

ABSTRACT

Ti metal treated with NaOH, NH₄OH, and heat and then soaked in simulated body fluid (SBF) showed in vitro apatite formation whereas that treated with NaOH, HNO₃, and heat and then soaked in SBF did not. The anatase TiO₂ precipitate and/or the fine network structure formed on the surface of the Ti metal treated with NaOH, NH₄OH, and heat and then soaked in SBF might be responsible for the formation of apatite on the surface of the metal. The NaOH, NH₄OH, and heat treatments might produce nitrogen-doped TiO₂ on the surface of the Ti metal, and the concentration of methylene blue (MB) in the Ti metal sample treated with NaOH, NH₄OH, and heat decreased more than in the untreated and NaOH- and heat-treated ones. This preliminary result suggests that Ti metal treated with NaOH, NH₄OH, and heat has the potential to show photocatalytic activity under visible light.

© 2013 Elsevier B.V. All rights reserved.

1. Introduction

Postoperative infection is a serious problem that occurs because of the growth of bacteria on the surface of metallic orthopedic implants. Although the incidence of surgical site infection (SSI) depends on the surgical sites themselves and on the operative procedures, it has previously been reported that the incidence of SSI for artificial hip joints was 0.2–0.6% [1–3] and for artificial knee joints was 2.2–2.9% [2,4,5]. When implants were externally fixed, the incidence of SSI was 51% [6]. Unfortunately when infection occurs, a surgical operation is essential to replace the implants at worst, resulting in a remarkable decrease in quality of life (QOL) for patients. Therefore, it is desirable to develop antibacterial, biocompatible metallic implants in order to minimize the incidence of SSI and thus minimize the need for implant replacement.

Numerous attempts have been made to develop antibacterial, biocompatible metallic implants including silver-coated [7,8] and silver-containing-hydroxyapatite-coated metallic implants [9,10]; however, silver is toxic to human cells [11,12]. Silver-free antibacterial metallic implants and iodine-supported titanium implants

were recently developed [13], and good clinical results have been reported [14].

About 15 years ago, treating titanium (Ti) metal and its alloys with sodium hydroxide (NaOH) and subsequently heating them [15] was found to induce bone bonding (i.e., bioactivity) on implants produced from them [16]. A NaOH- and heat-treated artificial hip joint produced from Ti–6Al–2Nb–Ta alloy was clinically used in Japan for the first time in 2007 [17]. However, because NaOH- and heat-treated Ti metal does not exhibit antibacterial properties, silver-doped bioactive Ti metal has recently been used as a material for implants [18] despite concerns about the cytotoxicity of silver.

It has previously been reported that sodium titanate and titania (TiO₂) containing rutile and anatase structures, which are formed on the surface of NaOH- and heat-treated Ti metal and its alloys, are responsible for the bioactivity [15]. Further, the TiO₂ layer that forms on Ti metal during anodic oxidation shows in vitro apatite formation [19,20] and in vivo bone bonding [21]. It has previously been reported that nitrogen (N)-doped TiO₂, on the other hand, shows visible-light-induced photocatalytic activity [22–24]. Therefore, if N atoms are successfully incorporated into the surface TiO₂ layer on Ti metal to induce photocatalytic activity with visible light, the resultant Ti metal would show not only in vivo bioactivity but also ex vivo visible-light-induced antibacterial properties such as those induced under shadowless light in an operation room. It is expected that either aqueous ammonia (NH₄OH) or nitric acid (HNO₃) could

* Corresponding author. Tel.: +81 22 795 3937; fax: +81 22 795 4735.
E-mail address: m-kawa@ecei.tohoku.ac.jp (M. Kawashita).

Table 1
Abbreviated names of samples subjected to various surface treatments.

Treatments	Abbreviated name
NaOH + heat	S-H
NaOH + NH₄OH	S-A
NaOH + NH₄OH + heat	S-A-H
NaOH + HNO₃	S-N
NaOH + HNO₃ + heat	S-N-H

be used to introduce N atoms into the surface of NaOH-treated Ti metal because the sodium-hydrogen-titanate-gel layer formed during NaOH treatment of Ti metal would be highly reactive. In this study, we investigated apatite formation and visible-light photocatalytic activity of Ti metal subjected to a series of treatments: NaOH, either aqueous ammonia (NH₄OH) or nitric acid (HNO₃), and heat. The results are discussed in terms of the structures on the surface of the treated Ti metal.

2. Materials and methods

2.1. Sample preparation

Commercially available pure Ti plates (10 mm × 10 mm × 1 mm; purity: 99.9%; Kojundo Chemical Laboratory, Japan) were used. They were abraded using No. 400 abrasive paper and then washed with pure acetone and ultrapure water in an ultrasonic cleaner. The Ti plates were soaked in 5 mL of 5 M NaOH solution at 60 °C. The samples were subsequently soaked in 7 mL of either 1 M NH₄OH or 1 M HNO₃ at 40 °C for 24 h and were then gently washed with ultrapure water and dried. Special grade NaOH (Wako Pure Chemical Industries, Japan), 28% NH₄OH (Wako Pure Chemical Industries, Japan), and HNO₃ (Wako Pure Chemical Industries, Japan) were used in this study. The samples were heated to 600 °C at a rate of 5 °C min⁻¹ in an electric furnace (MSFS-1218, Yamada Denki, Japan), maintained at this temperature for 1 h, and then naturally cooled to room temperature in the furnace. The abbreviated names of the samples subjected to various treatments are listed in Table 1.

2.2. Immersion of samples in simulated body fluid

The samples were soaked in 30 mL of simulated body fluid (SBF) [25,26] containing ion concentrations (Na⁺: 142.0 mM; K⁺: 5.0 mM; Ca²⁺: 2.5 mM; Mg²⁺: 1.5 mM; Cl⁻: 147.8 mM; HCO₃⁻: 4.2 mM; HPO₄²⁻: 1.0 mM; SO₄²⁻: 0.5 mM) that were nearly identical to those in human blood plasma at 36.5 °C, according to the ISO 23317:2007 standard. After the samples had been immersed in SBF for 7 d, they were removed and gently washed with ultrapure water.

2.3. Characterization of sample surfaces

The surface structures of the samples were investigated using a thin-film X-ray diffractometer (TF-XRD; RINT-2200VL, Rigaku, Japan), scanning electron microscope (SEM; VE-8800, Keyence, Japan), and an X-ray photoelectron spectrometer (XPS; AXIS Ultra DLD, Kratos Analytical, U.K.). We used the following settings during the TF-XRD measurements. X-ray source: Ni-filtered Cu Kα radiation; X-ray power: 40 kV, 40 mA; scanning rate: 2° min⁻¹; sampling angle: 0.02°. We used the following settings during the XPS measurements. X-ray source: monochromatic Al Kα radiation (1486.7 eV); X-ray power: 15 kV, 10 mA. The binding energy was calibrated using the C₁ₛ photoelectron peak at 284.8 eV as a reference. The XPS peak analysis was performed using CasaXPS Version 2.3.15 software with all spectra Shirley background subtracted prior to fitting. The elemental composition was calculated from XPS
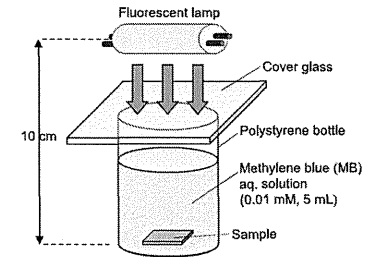

Fig. 1. Schematic illustration of apparatus used to evaluate visible-light photocatalytic activity.

spectra using the specific relative sensitivity factors for the Kratos Axis Ultra (O₁ₛ: 0.78, Ti₂ₚ: 2.001, N₁ₛ: 0.477, C₁ₛ: 0.278).

2.4. Evaluation of visible-light photocatalytic activity

The visible-light photocatalytic activity of the samples was evaluated by examining the decomposition of methylene blue (MB; Waldeck, Germany), which is often used as a model substance. The samples were soaked in 5 mL of 0.01 mM MB aqueous solution and incubated for 24 h to reach adsorption equilibrium. The MB aqueous solution was then replenished, and the samples were irradiated with 400–700 nm wavelength fluorescent light (FPL27EX-N, Panasonic, Japan) for 6 h. The distance between the fluorescent light and the samples was fixed at 10 cm. Here, it is noted that the wavelength of the fluorescent light (400–700 nm) should be similar to that of light source in operation room, but the distance between fluorescent light and samples (10 cm) is not possible in operation room. However, in the present study, we aimed to investigate visible-light photocatalytic activity of samples fundamentally. Fundamental findings on the visible-light photocatalytic activity of samples can be obtained even in the present experimental condition. In future study, we should carry out the experiment under the real condition in operation room. The MB concentration in the irradiated samples was examined using an ultraviolet visual (UV–VIS) spectrophotometer (Sefi IUV-1240, As One, Japan) by measuring the UV absorbance at 664 nm. A schematic illustration of the apparatus is shown in Fig. 1. The MB concentration was also measured in unsoaked samples as a control. The decrease in MB concentration (%) was calculated based on the difference in the concentration of MB in the soaked and unsoaked samples, C_{sample} and C_{blank}, respectively, as follows [27]:

$$\text{Decrease in concentration}(\%) = \frac{(C_{blank} - C_{sample}) \times 100}{C_{blank}} \quad (1)$$

3. Results and discussion

Fig. 2(a) shows SEM photographs of samples of Ti metal subjected to various surface treatments. A fine network structure had formed on the surface of the S-A-H sample, similar to that previously reported on the surface of the S-H sample [15]. In contrast, the untreated Ti metal and the S-N-H samples exhibited flat surfaces. Fig. 2(b) shows TF-XRD patterns for the Ti metal samples subjected to various treatments. The pattern for the S-H sample displayed TF-XRD peaks ascribed to Ti (PDF #44-1294), sodium titanate (Na₂Ti₅O₁₁) (PDF #11-0289), rutile TiO₂ (PDF #21-1276), and anatase TiO₂ (PDF #21-1272). TF-XRD peaks associated with Ti, anatase TiO₂, and rutile TiO₂ were observed in the pattern for the

(a)

(b)

Fig. 2. SEM photographs (a) and TF-XRD patterns (b) of Ti metal subjected to various surface treatments.
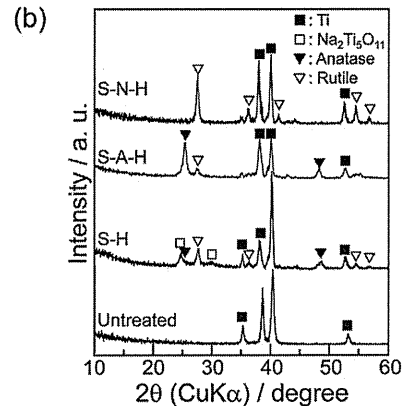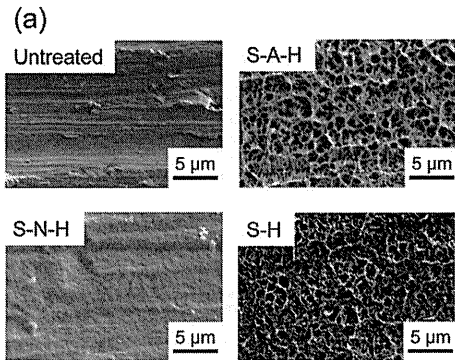
Fig. 3. TF-XRD patterns for samples S-A and S-N.

S-A-H sample, and those associated with Ti and rutile TiO$_2$ were observed in the pattern for the S-N-H sample. Fig. 3 shows TF-XRD patterns for the S-A and S-N samples. The pattern for the S-A sample showed TF-XRD peaks associated with Ti, sodium hydrogen titanate (Na$_x$H$_{2-x}$Ti$_3$O$_7$) [28,29], and anatase TiO$_2$, whereas the pattern for the S-N sample only showed peaks associated with Ti. The experimental results shown in Figs. 2(a) and 3 suggest that although the surface layer formed during NaOH treatment was completely dissolved in 1 M HNO$_3$ [29], it persisted even after NH$_4$OH treatment. In fact, it has previously been reported that sodium titanate nanowire was dissolved under acidic conditions such as in 1 M HCl [30]. Further, according to the results shown in Figs. 2(b) and 3, we can speculate that the rutile TiO$_2$ on the surface of the S-N-H sample was formed during simple thermal oxidation of Ti metal and that although a very small amount of Na$_2$Ti$_5$O$_{11}$ might be formed during subsequent heat treatment, the Na$_x$H$_{2-x}$Ti$_3$O$_7$ that had formed on the surface of the S-A sample was transformed into anatase and rutile TiO$_2$ [31].

Fig. 4 shows XPS spectra containing Na$_{KLL}$, Ti$_{2p}$, O$_{1s}$, and N$_{1s}$ peaks associated with samples of Ti metal subjected to various

surface treatments. The Na$_{KLL}$ XPS peak ascribed to the Na–O bond [32] was observed at around 495 eV in the spectra for the S-H and S-A-H samples; however, the intensity of the peak changed depending on the surface treatment. The peak was not observed in the spectrum for the S-N-H sample. We estimated from the areas under the Na$_{KLL}$ XPS peaks that the concentrations of Na on the surfaces of the S-H and S-A-H samples were 10.36 ± 1.40 and 2.93 ± 1.97 at.%, respectively. We observed that the concentration of Na remarkably decreased on the surfaces of the samples treated with either NH$_4$OH or HNO$_3$. The spectra for all samples showed Ti$_{2p}$ XPS peaks at around 457.9 and 464.8 eV, which were ascribed to TiO$_2$ [33]. The spectra also showed an O$_{1s}$ XPS peak ascribed to TiO$_2$ [33] at around 529 eV [33] and a shoulder ascribed to OH [34] at around 530.6 eV. The concentrations of OH on the surfaces of the S-H, S-A-H, and S-N-H samples were calculated as 5.76 ± 0.61, 7.60 ± 1.02, and 9.73 ± 0.34 at.%, respectively. We observed that although the concentration of OH increased on the surfaces of the samples treated with either NH$_4$OH or HNO$_3$, the former developed apatite whereas the latter did not. Although numerous studies have previously indicated that Ti–OH groups induced apatite nucleation [35–38], no correlation was found between the concentrations of Na and OH on the surfaces of the samples and formation of apatite in our study. The spectra for the S-H and S-A-H samples showed a single N$_{1s}$ peak at around 399.5 eV, whereas that for the S-N-H sample showed two N$_{1s}$ peaks at around 399.5 and 401 eV. The peak at around 399.5 eV was ascribed either to nitrogen dopant incorporated into TiO$_2$ as interstitial and/or impurity N atoms or to O–Ti–N, and the one at around 401 eV was ascribed to surface-adsorbed NO [39–42]. The concentrations of N on the surfaces of the S-H, S-A-H, and S-N-H samples were calculated as 0.64 ± 0.40, 0.16 ± 0.02, and 1.10 ± 0.03 at.%, respectively. Here, we note that the concentration of the impurity N on the surface of the untreated Ti plates was around 2.96 at.%. These results suggest that the impurity N partially dissolved in the NaOH and that although the concentration of N on the surface was further decreased, N-doped TiO$_2$ might be formed when the samples were subsequently treated with either NH$_4$OH or HNO$_3$. We cannot provide convincing explanation on the reason why the nitrogen can be entered into the surface TiO$_2$ by either NH$_4$OH or HNO$_3$ treatment. But, we consider that either NH$_4$OH or HNO$_3$ could be used to introduce N atoms into the surface of NaOH-treated Ti metal, because the sodium-hydrogen-titanate (Na$_x$H$_{2-x}$Ti$_3$O$_7$) gel layer formed during NaOH treatment of Ti metal would be highly reactive and it is reported that N-doped TiO$_2$ can be obtained by aqueous ammonia solution treatment of TiO$_2$-based materials [43].

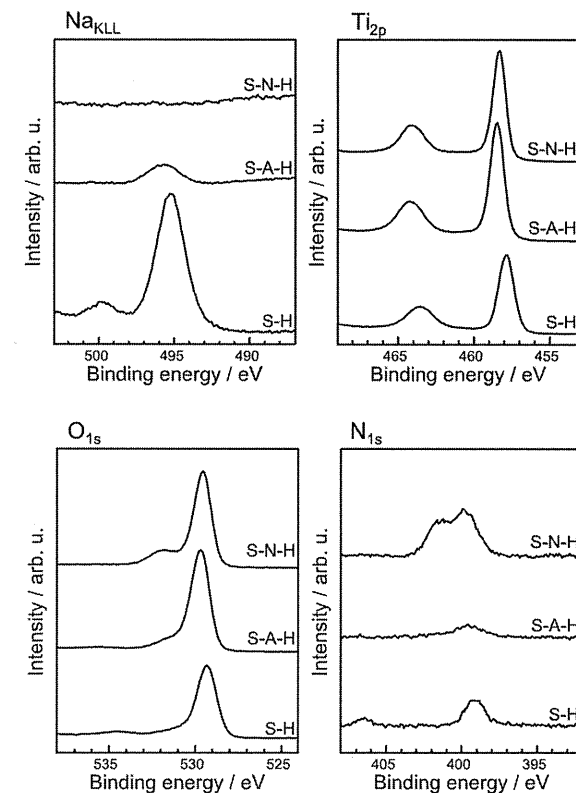Fig. 4. XPS spectra containing Na$_{KLL}$, Ti$_{2p}$, O$_{1s}$, and N$_{1s}$ peaks for Ti metal subjected to various surface treatments.

Fig. 5 shows SEM photographs (a) and TF-XRD patterns (b) for samples of Ti metal subjected to various treatments and then soaked in SBF for 7 d. Apatite formed on the surfaces of the S-H and S-A-H samples; however, it did not form on the surface of the S-N-H sample. Although the extent of the formation of apatite on the surface of the S-A-H sample was slightly less than that of the formation of apatite on the surface of the S-H sample, the present results suggest that the sample of Ti metal treated with NaOH, NH$_4$OH, and heat has the potential to show in vivo bioactivity. Here, we note that although apatite did not form on the surface of the S-N-H sample, even after it was soaked in SBF for 7 d in the present study, it did form on the surface of the Ti metal sample soaked in SBF

within 1 d, even after the sample was treated with NaOH, HNO$_3$, and heat according to the previous report [29]. The difference in the concentration of HNO$_3$ (present study: 1 M; previous study: 0.5–100 mM) might be responsible for the remarkable difference in the formation of apatite on the surfaces of the samples. That is, the surface structure produced when the sample was treated with NaOH might have partially remained when the sample was subsequently treated with HNO$_3$ in previous study, whereas the surface structure might have completely dissolved in HNO$_3$, as can be seen from Fig. 3, because the concentration of HNO$_3$ was as high as 1 M in the present study. Table 2 summarizes crystalline phases, Na, Ti–OH, and N contents, and formation of apatite on the

Table 2
Crystalline phases, Na, Ti–OH, and N contents (mean ± SD, n = 5), and formation of apatite on surfaces of samples subjected to various surface treatments and then soaked in SBF (R: rutile, A: anatase, ST: sodium titanate).

Sample	Crystalline phase	Na content (at.%)	Ti–OH content (at.%)	N content (at.%)	Apatite formation in SBF
S-N-H	Ti, R	0.04 ± 0.02	9.73 ± 0.34	1.10 ± 0.03	No
S-A-H	Ti, A, R	2.93 ± 1.97	7.60 ± 1.02	0.16 ± 0.02	Yes
S-H	Ti, ST, A, R	10.36 ± 1.40	5.76 ± 0.61	0.64 ± 0.40	Yes

Fig. 6. Decrease in concentration of MB due to irradiating immersed samples with visible light (mean ± SD, $n = 5$).

Fig. 4 and Table 2). We speculate that the precipitation of anatase TiO_2 on sample would play some role in the expression of visible-light-induced photocatalytic activity. In fact, as can be seen in Fig. 2(b), anatase TiO_2 mainly precipitated on the surface of the S-A-H, whereas $Na_2Ti_5O_{11}$ and rutile TiO_2 mainly precipitated with the S-H sample. Although further detailed investigation of this phenomenon is required because not only the surface structure but also the surface area of the samples would affect the results of the evaluation of the visible-light photocatalytic activity, this preliminary result suggests that the S-A-H sample has the potential to show photocatalytic activity under visible light. Antibacterial activity test is important to directly indicate the usefulness of the S-A-H sample. However, further optimizing of condition of NaOH, NH₄OH, and heat treatments is needed prior to antibacterial activity test, because only one treatment condition was used in this study. Now we are finding the optimal treatment condition and hence we believe to report the antibacterial activity of samples in future work. In conclusion, treating the samples with NaOH, NH₄OH, and heat is useful for forming apatite on the surface of Ti metal and for producing photocatalytic activity of Ti metal under visible light. Achieving these two properties would provide novel bioactive Ti metal that exhibits antibacterial properties when subjected to visible light.

4. Conclusions

Ti metal sample treated with NaOH, NH₄OH, and heat and then soaked in SBF showed *in vitro* formation of apatite on the surface of the metal whereas that treated with NaOH, HNO₃, and heat did not. The anatase-TiO_2 precipitate and/or the fine network structure formed on the surface of the Ti metal sample treated with NaOH, NH₄OH, and heat and soaked in SBF might be responsible for the formation of apatite on the surface of the metal. A small amount of nitrogen was on the surface of the Ti metal sample treated with NaOH, NH₄OH, and heat, and the concentration of MB in that sample decreased more than in the untreated and NaOH- and heat-treated ones. The present results suggest that Ti metal treated with NaOH, NH₄OH, and heat has the potential to show bioactivity and photocatalytic activity under visible light.
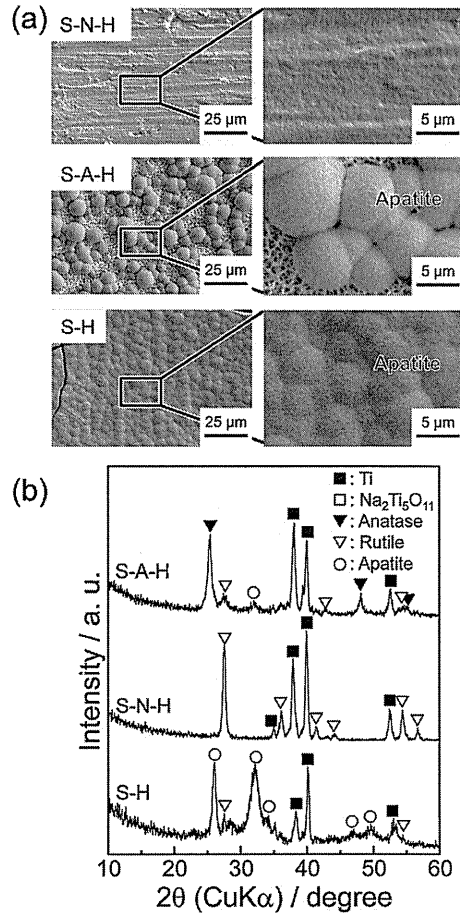
Acknowledgements

Fig. 5. SEM photographs (a) and TF-XRD patterns (b) of Ti metal subjected to various surface treatments and then soaked in SBF for 7 d.

surfaces of samples subjected to various treatments and then soaked in SBF. According to the results shown in Table 2 and Fig. 2, the anatase TiO_2 [44,45] and/or the fine network structure formed on the surface of the Ti metal sample treated with NaOH, NH₄OH, and heat are/is considered to be responsible for the formation of apatite on the surface of the sample soaked in SBF although the detailed mechanism for the formation of apatite is still unclear.

Fig. 6 shows the decrease in the concentration of MB in samples immersed in MB solution and irradiated with visible light. The concentration of MB in the S-A-H sample decreased more than that in the untreated and S-H samples. It is interesting that S-A-H sample gave slightly better visible-light photocatalytic activity than S-H sample although the concentration of N on the surface of the S-A-H sample was smaller than that of the S-H sample (see
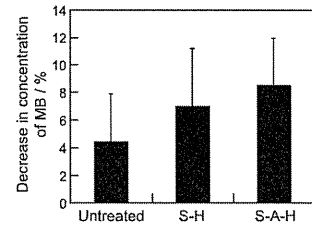
References

[1] G.E. Hill, D.G. Droller, Orthop. Rev. 18 (1989) 617.
[2] A.B. Wymenga, J.R. van Horn, A. Theeuwes, H.L. Muytjens, T.J. Slooff, Acta Orthop. Scand. 63 (1992) 665.
[3] C.B. Phillips, J.A. Barrett, E. Losina, N.N. Mahomed, E.A. Lingard, E. Guadagnoli, J.A. Baron, W.H. Harris, R. Poss, J.N. Katz, J. Bone Joint Surg. Am. 85-A (2003) 20.
[4] S. Bengtson, K. Knutson, Acta Orthop. Scand. 62 (1991) 301.
[5] R.S. Petrie, A.D. Hanssen, D.R. Osmon, D. Ilstrup, Am. J. Orthop. 27 (1998) 172.
[6] G. Magyar, S. Toksvig-Larsen, A. Lindstrand, J. Bone Joint Surg. Br. 81 (1999) 449.
[7] M. Bosetti, A. Masse, E. Tobin, M. Cannas, Biomaterials 23 (2002) 887.
[8] G. Gosheger, J. Hardes, H. Ahrens, A. Streitburger, H. Buerger, M. Erren, A. Gunsel, F.H. Kemper, W. Winkelmann, C. von Eiff, Biomaterials 25 (2004) 5547.
[9] W. Chen, Y. Liu, H.S. Courtney, M. Bettenga, C.M. Agrawal, J.D. Bumgardner, J.L. Ong, Biomaterials 27 (2006) 5512.
[10] I. Noda, F. Miyaji, Y. Ando, H. Miyamoto, T. Shimazaki, Y. Yonekura, M. Miyazaki, M. Mawatari, T. Hotokebuchi, J. Biomed. Mater. Res. Part B: Appl. Biomater. 89B (2009) 456.
[11] C.N. Kraft, M. Hansis, S. Arens, M.D. Menger, B. Vollmar, J. Biomed. Mater. Res 49 (2000) 192.
[12] A. Masse, A. Bruno, M. Bosetti, A. Biasibetti, M. Cannas, P. Gallinaro, J. Biomed. Mater. Res. 53 (2000) 600.
[13] T. Shirai, T. Shimizu, K. Ohtani, Y. Zen, M. Takaya, H. Tsuchiya, Acta Biomater. 7 (2011) 1928.
[14] H. Tsuchiya, T. Shirai, H. Nishida, H. Murakami, T. Kabata, N. Yamamoto, K. Watanabe, J. Nakase, J. Orthop. Sci. 17 (2012) 595.
[15] H.-M. Kim, F. Miyaji, T. Kokubo, T. Nakamura, J. Biomed. Mater. Res. 32 (1996) 409.
[16] W.-Q. Yan, T. Nakamura, M. Kobayashi, H.-M. Kim, F. Miyaji, T. Kokubo, J. Biomed. Mater. Res 37 (1997) 267.
[17] T. Kokubo, H. Takadama, M. Matsushita, in: T. Kokubo (Ed.), Bioceramics and Their Clinical Applications, Woodhead Pub. Ltd., Cambridge, 2008 (Chapter 21).
[18] T. Kizuki, T. Matsushita, T. Kokubo, in: M. Niinomi (Ed.), Development of Antibacterial Bioactive Ti Metal and its Alloy, Proc. 2012 Symposium Japanese Society for Biomaterials, Sendai, November 27, Japanese Society for Biomaterials Symposium 2012, Sendai, 2012, p. 250.
[19] B.C. Yang, M. Uchida, H.-M. Kim, X.D. Zhang, T. Kokubo, Biomaterials 25 (2004) 1003.
[20] X. Cui, H.-M. Kim, M. Kawashita, L. Wang, T. Xiong, T. Kokubo, T. Nakamura, Dent. Mater. 25 (2009) 80.

[21] B. Liang, S. Fujibayashi, M. Neo, J. Tamura, H.-M. Kim, M. Uchida, T. Kokubo, T. Nakamura, Biomaterials 24 (2003) 4959.
[22] S. Sato, Chem. Phys. Lett. 123 (1986) 126.
[23] R. Asahi, T. Morikawa, T. Ohwaki, K. Aoki, Y. Taga, Science 293 (2001) 269.
[24] R. Bacsa, J. Kiwi, T. Ohno, P. Albers, V. Nadtochenko, J. Phys. Chem. B 109 (2005) 5994.
[25] S.B. Cho, K. Nakanishi, T. Kokubo, N. Soga, C. Ohtsuki, T. Nakamura, T. Kitsugi, T. Yamamuro, J. Am. Ceram. Soc. 78 (1995) 1769.
[26] T. Kokubo, H. Takadama, Biomaterials 27 (2006) 2907.
[27] M. Kamitakahara, O. Kawaguchi, N. Watanabe, K. Ioku, Mater. Res. Bull. 46 (2011) 2283.
[28] X. Sun, Y. Li, J. Chem. Eur. 9 (2003) 2229.
[29] D.K. Pattanayak, S. Yamaguchi, T. Matsushita, T. Kokubo, J. Mater. Sci.: Mater. Med. 22 (2011) 1803.
[30] B. Schürer, M.J. Elser, A. Sternig, W. Peukert, O. Diwald, J. Phys. Chem. C 115 (2011) 12381.
[31] S. Papp, L. Körösi, V. Meynen, P. Cool, E.F. Vansant, I. Dékány, J. Solid State Chem. 178 (2005) 1614.
[32] A. Barrie, F.J. Street, J. Electron. Spectrosc. Relat. Phenom. 7 (1975) 1.
[33] F.A. Akin, H. Zreiqat, S. Jordan, M.B.J. Wijesundara, L. Hanley, J. Biomed. Mater. Res. 57 (2001) 588.
[34] Y. Nakao, A. Sugino, K. Tsuru, K. Uetsuki, Y. Shirosaki, S. Hayakawa, A. Osaka, J. Ceram. Soc. Jpn. 118 (2010) 483.
[35] P. Li, C. Ohtsuki, T. Kokubo, K. Nakanishi, N. Soga, T. Nakamura, T. Yamamuro, K. de Groot, J. Biomed. Mater. Res. 28 (1994) 7.
[36] T. Kasuga, H. Kondo, M. Nogami, J. Cryst. Growth. 235 (2002) 235.
[37] T. Kokubo, H.-M. Kim, M. Kawashita, Biomaterials 24 (2003) 2161.
[38] H. Maeda, T. Kasuga, M. Nogami, J. Eur. Ceram. Soc. 24 (2004) 2125.
[39] X. Chen, Y.-B. Lou, A.C.S. Samia, C. Burda, J.L. Gole, Adv. Func. Mater. 15 (2005) 41.
[40] M. Sathish, B. Viswanathan, R.P. Viswanath, C.S. Gopinath, Chem. Mater. 17 (2005) 6349.
[41] G. Liu, H.G. Yang, X. Wang, L. Cheng, J. Pan, G.Q. Lu, H.-M. Cheng, J. Am. Chem. Soc. 131 (2009) 12868.
[42] J. Zhang, J. Xi, Z. Ji, J. Mater. Chem. 22 (2012) 17700.
[43] T. Matsumoto, N. Iyi, Y. Kaneko, K. Kitamura, Y. Takasu, Y. Murakami, Chem. Lett. 5 (2004) 1508.
[44] T. Kawai, T. Kizuki, H. Takadama, T. Matsushita, H. Unuma, T. Nakamura, T. Kokubo, J. Ceram. Soc. Jpn. 118 (2010) 19.
[45] M. Kawashita, N. Matsui, T. Miyazaki, H. Kanetaka, Mater. Trans. 54 (2013) 811.

Collagenase H is crucial for isolation of rat pancreatic islets

Atsushi Fujio[1], Kazutaka Murayama[2], Youhei Yamagata[3], Kimiko Watanabe[4], Takehiro Imura[4], Akiko Inagaki[4], Naomi Ohbayashi[2,5], Hiroki Shima[6], Satoshi Sekiguchi[1], Keisei Fujimori[1], Kazuhiko Igarashi[6], Noriaki Ohuchi[1], Susumu Satomi[1], and Masafumi Goto[1,4]

[1]*Division of Advanced Surgical Science and Technology, Tohoku University, Sendai, 980-0872, Japan*

[2]*Graduate school of Biomedical Engineering, Tohoku University, 980-0872, Sendai, Japan*

[3]*Graduate school of Agricultural Science, Tokyo University of Agriculture and Technology, Tokyo, 183-8531, Japan*

[4]*New Industry Creation Hatchery Center, Tohoku University, Sendai, 980-0872, Japan*

[5]*Faculty of pharmacy, Iwaki Meisei University, Iwaki, 970-8551, Japan*

[6]*Graduate school of Medicine, Tohoku University, Sendai, 980-0872, Japan*

Running head: The importance of collagenase H in islet isolation

Address for correspondence:

Masafumi Goto, M.D., Ph. D.

New Industry Creation Hatchery Center,

Tohoku University

1-1 Seiryo-machi, Aoba-ku, Sendai, Miyagi, 980-0872, Japan

Tel : +81 22 717 7895

Fax : +81 22 717 7899

E-mail : gotokichi@aol.com

Abstract

Background: The role(s) of Collagenase G (ColG) and Collagenase H (ColH) during pancreatic islet isolation remain controversial, possibly due to the enzyme blends used in the previous studies. We herein examined the role of ColG and ColH using highly pure enzyme blends of recombinant collagenase of each subtype.

Methods: Rat pancreases were digested using thermolysin, together with ColG, ColH, or ColG/ColH (n=9, respectively). No tryptic-like activity was detected in any components of the enzyme blends. The efficiency of the collagenase subtypes was evaluated by islet yield and function. An immunohistochemical analysis, *in vitro* collagen digestion assay, and mass spectrometry were also performed to examine the target matrix components of the crucial collagenase subtype.

Results: The islet yield in the ColG/ColH group was the highest (4,101 ± 460 islet equivalents). A substantial number of functional islets (2,811 ± 581 islet equivalents) were obtained in the ColH group, whereas no islets were retrieved in the ColG group. Mass spectrometry demonstrated that ColH reacts with collagen-I and III. In the immunohistochemical analysis, both collagen-I and III were located in exocrine tissues, although collagen-III expression was more pronounced. The collagen digestion assay showed that collagen-III was more effectively digested by ColH than by ColG.

Conclusions: The present study reveals that ColH is crucial, while ColG plays only a supporting role, in rat islet isolation. In addition, collagen-III appears to be one of the key targets of ColH.

Key words: islet isolation, diabetes mellitus, collagenase, collagen, mass spectrometry

Abbreviations

ADP, adenosine diphosphate

ANOVA, analysis of variance

ATP, adenosine triphosphate

AUC, area under the curve

ColG, Collagenase G

ColH, Collagenase H

DNA, deoxyribonucleic acid

ECM, extracellular matrix

E. coli, *Escherichia coli*

FALGPA, 2-furanacryloyl-L-leucylglycyl-L-prolyl-L-alanine

HBSS, Hanks' balanced salt solutions

HEPES, 4-(2-hydroxyethyl)-1-piperazineethanesulfonic acid

IEQs, islet equivalents

IPGTT, intraperitoneal glucose tolerance test

PAGE, polyacrylamide gel electrophoresis

PBS, phosphate-buffered saline

PCR, polymerase chain reaction

Pz-PLGPR, 4-phenylazobenzyloxycarbonyl-Pro-Leu-Gly-Pro-D-Arg

SD, standard deviation

SDS, sodium dodecyl sulfate

SGS, static glucose stimulation

SI, stimulation index

TL, thermolysin

TLA, tryptic-like activity

TMPP, (N-Succinimidyloxycarbonylmethyl) tris (2,4,6-trimethoxyphenyl) phosphonium bromide

Introduction

Pancreatic islet transplantation is a promising treatment for restoring normoglycemia in type 1 diabetic patients (24,27,28). However, there are still many issues to be resolved regarding this treatment. One is that two or more donor pancreases are needed to render one diabetic patient insulin-independent. Considering the organ shortage, a more efficient isolation procedure is needed, wherein a large number of high quality islets can be stably obtained from one donor pancreas. Although several factors are related to the outcome of islet isolation (12,19,21,23), the enzymes used for digestion are one of the crucial factors (12,17,21).

To isolate islets, the pancreatic tissue first has to be dissociated by enzymatic degradation of the extracellular matrix (ECM) without damaging the structural and functional integrity of the islets. Crude collagenase preparations from *Clostridium histolyticum*, which have been routinely used for this purpose, are complex mixtures of different collagenases, neutral protease, and various other enzymes that possess tryptic-like activity (TLA) (8,32). Although highly purified collagenases are readily available in recent clinical islet isolations, these enzymes still contain certain level of TLA. The original crude collagenase preparations contain at least six different collagenases with molecular weights ranging from 68 to 125 kDa (4,5). On the basis of their activities toward native collagen and the synthetic peptide 2-furanacryloyl-L-leucylglycyl-L-prolyl-L-alanine (FALGPA), the six collagenases are divided into two classes. Collagenase G (ColG) (corresponding to Class I collagenases) has high collagenase activity and moderate FALGPA activity, while Collagenase H (ColH) (corresponding to Class II collagenases) has moderate collagenase and high FALGPA activity (4-6).

The role of the collagenase subtypes has been examined in several studies, but still remains controversial. An early study of rat islet isolation suggested that ColH plays a more important role (32), while another study showed that equal amounts of ColG and ColH were required for efficient rat islet isolation (7). Barbara et al. reported that, in human islet isolation, ColH was correlated with the

islet yield and digestion time (1). Conversely, Kin et al. reported that a ColH/ColG ratio < 0.204 resulted in a high islet yield (17).

A possible explanation for these discrepancies is the enzymes used in each study. In most of the previous studies, crude collagenases produced by *Clostridium histolyticum* were purified and fractionated by anion exchange chromatography (1,9,32). Therefore, a risk of contamination with an unwanted collagenase subtype or unknown proteases derived from *Clostridium histolyticum* could not be ruled out. The use of highly purified recombinant collagenase of each subtype could help to overcome this problem. In fact, Wolters et al. (32) reported that the pancreas dissociation was different between chromatographically-purified ColG and recombinant ColG. Of particular interest, Brandhorst et al. (9) recently reported that TLA also facilitates islet isolation (8). This novel finding suggests that some unknown protease(s) other than collagenases and neutral protease may affect pancreas dissociation, since collagenases and neutral protease are known to have no TLA. Hence, TLA-free enzyme preparations should be used to investigate the roles of specific collagenase subtypes.

Another possible explanation for the discrepancies among the previous studies is the difference in the pancreatic ECM among species (15,29). A broad variation of the ECM is also seen in individual human pancreases (3,16,25,30). Therefore, elucidating the target ECM of each collagenase subtype would be beneficial not only for investigating the role of the two types of collagenase, but also for optimizing the outcome of islet isolation.

The present study examined the roles of ColG and ColH in islet isolation using TLA-free enzyme preparations of highly purified recombinant collagenase of each subtype. We also investigated the molecular composition of the target ECM in rat pancreases of the crucial collagenase subtype using an immunohistochemical analysis and mass spectrometry.

Materials and Methods

Animals

Rat pancreases were obtained from 10-week-old male inbred Lewis rats (Japan SLC Inc., Shizuoka, Japan) weighing 265 to 300 g. All animals used in this study were handled in accordance with the Guide for the Care and Use of Laboratory Animals published by the National Institutes of Health (2) and the guidelines for animal experiments and related activities at Tohoku University (approved protocol ID: 2012 NICHe-Animal-5). All surgeries were performed under anesthesia, and maximal efforts were made to minimize suffering.

Construction of ColG-His and ColH-His expression systems

The coding region of ColG was amplified with a colG-F primer and colG-R primer. The primers used in the present study are shown in Table 1. The genomic deoxyribonucleic acid (DNA) from *Clostridium histolyticum* was used as a template. As a result of the substitutions, the amino acid residues at 1007-1008 were changed from Asn-Lys to Ser-Arg. The promoter region of the *lacZ* gene was amplified with lac-F and lac-R primers, and the plasmid (pUC19) was used as a template. The polymerase chain reaction (PCR) fragment for ColG was digested with *Bam*HI, and the promoter fragment was digested with *Hind*III. Both digested fragments were inserted into the plasmid, pBR322, which was digested with *Bam*HI and *Hind*III (lacZ-ColG-pBR322). The His-tag coding region and following multi-cloning site of pET24a (Novagen, Darmstadt, Germany) were amplified with a set of primers for His-F and His-R. The PCR fragments were digested with *Bam*HI and *Xba*I. The digested DNA fragments were inserted into the plasmid described above (*lacZ*-ColG-His-tag-pBR322), digested with *Bam*HI and *Xba*I. The expression plasmid for the collagenase H-His-tag fusion protein was constructed using the same method described above, with the exception of the PCR for the ColH coding sequence. The coding region of ColH was amplified with colH-F and colH-R primers. The

amino acid residue [980]Gly in ColH was substituted with [980]Ala. The plasmids, pColG-His and pColH-His, were used for the transformation of *Escherichia coli (E. coli)* χ1176.

Enzyme production and purification

The *E. coli* carrying pColG-His or pColH-His were cultured in 100 mL of Terrific Broth (1.2% tryptone, 2.4% yeast extract, 0.94% K_2HPO_4, 0.22% KH_2PO_4, 0.8% glycerol) containing 100 μg/mL 2, 4-diaminopimeric acid, 20 μg/mL thymidine, 50 μg/mL ampicillin and 0.1 mM isopropyl β-D-1-thiogalactopyranoside at 28°C for 16 h. Ten milliliters of POPculture reagent (Merck-Millipore, Darmstadt, Germany) were added to the culture broth and mixed well. The mixture was filtered with a 0.2 μm cellulose acetate filter to remove any remaining bacteria. A six-fold volume of binding buffer (20 mM phosphate buffer pH 7.5 containing 0.5 M NaCl, and 20 mM imidazole) was added to the filtrate. The mixture was applied to a 100 mL of Ni-NTA agarose column (Qiagen, Duesseldorf, Germany). The column was washed adequately with binding buffer, and then the enzyme was eluted with the same buffer excluding 500 mM imidazole. The collected His-tagged ColG and ColH were dialyzed against 24.1 mM 4-(2-hydroxyethyl)-1-piperazineethanesulfonic acid (HEPES)- Hanks' Balanced Salt Solution (HBSS) at pH 7.6 and were concentrated with a Pellicon 3 cassette ultrafilteration module (Merck-Millipore).

Enzyme activity and blending

In the present study, recombinant ColG, ColH, and thermolysin (TL) (as a neutral protease) (Peptide institution Inc., Osaka, Japan) were used to prepare highly pure, TLA-free, enzyme blends. The enzyme blend activity was adjusted to equal that of the crude collagenase from *Clostridium histolyticum* (SIGMA collagenase type V) (Sigma Chemicals, St. Louis, MO) using Azocoll, 4-phenylazobenzyloxycarbonyl-Pro-Leu-Gly-Pro-D-Arg (Pz-PLGPR) and Azocasein as substrates (Table 2). The crude collagenase was just used as one example to decide the effective amount of ColG

and ColH. The TLA activity was measured by the cleavage of Bz-Arg-pNA (Wako Pure Chemical Industries, Ltd., Osaka, Japan) at 37°C and pH 7.5. Notably, no TLA was detected in any components of the enzyme blends. In all the experimental groups, 0.3 mg of TL was added. The GH group contained ColG and ColH. The G and H groups consisted of ColG or ColH, respectively.

Islet isolation

Rat islet isolation was performed as described previously (26). In brief, before the removal of the pancreas, the cannulated bile duct was injected with 10 mL of cold HBSS containing enzyme blends. After digestion at 37°C for 14 min, density-gradient centrifugation was performed using Histopaque-1119 (Sigma Diagnostics, St. Louis, MO) and LymphoprepTM (Nycomed Pharma AS, Oslo, Norway) to isolate the pancreatic islets. The islet count was performed as IEQs under a scaled microscope using diphenylthiocarbazone (Wako Pure Chemical Industries) staining. The islets were cultured in RPMI-1640 containing 5.5 mmol/L glucose and 10% fetal bovine serum at 37°C in 5% CO_2 and humidified air for three hours before examination.

In vitro and in vivo evaluation of islet function

Both the adenosine diphosphate (ADP)/adenosine triphosphate (ATP) ratio and the ATP/DNA ratio were measured to evaluate the energy status of the cultured islets. After picking up 80 islet equivalents (IEQs), the ApoGlow[TM] kit (Lonza Rockland Inc., Rockland, ME) was used for the ADP and ATP measurements, as described previously (13). Using the same sample, the DNA content was measured using a DNA Quantify kit (Primary cell, Ishikari, Japan) as described (31). The insulin/DNA ratio was measured as described previously (31). The *in vivo* islet function was assessed in nude mice (Japan SLC Inc.) rendered diabetic by an intravenous injection of 237.5 mg/kg streptozotocin (Sigma-Aldrich, St. Louis, MO) six days before transplantation of 700 IEQs under the left kidney capsule (n=6). Mice whose nonfasting blood glucose levels exceeded 400 mg/dL in two consecutive

measurements were considered diabetic. After transplantation, nonfasting blood glucose levels less than 200 mg/dL on two consecutive measurements were defined as normoglycemic and were considered to indicate graft function. The intraperitoneal glucose tolerance test (IPGTT) was performed 30 days after islet transplantation. After a 14 h fast, D-glucose (2.0 g/kg) was infused intraperitoneally as a single bolus, and the blood glucose concentrations were determined before and at 1, 3, 5, 10, 15, 20, 25, 30, 45, 60, 90 and 120 min after the glucose injection. The results of the IPGTT were evaluated by the area under the curve (AUC) and Kg values. Nephrectomy of the left kidneys was performed 35 days after transplantation to demonstrate the immediate return of hyperglycemia.

Sequential injection of collagenase subtypes into the pancreatic duct

This procedure examined the role of the collagenase subtypes in islet isolation. Briefly, two enzyme injections were made into the pancreatic ducts. Before the removal of the pancreas, the first enzyme blend was injected into the bile duct. After the addition of 10 ml HBSS, the pancreas was digested at 37°C for 7 min. Then, we added HBSS with the second enzyme blend, and again digested the pancreas at 37°C for 7 min. Density gradient centrifugation was performed to isolate the pancreatic islets.

Pancreatic tissue digestion and mass spectrometry analysis

Small pieces of Lewis pancreas (~100 mg) were incubated in 20 mM HEPES (pH8.0) and 1 mM $CaCl_2$ containing protease inhibitor cocktail (Roche, Basel, Switzerland) at 37°C (overnight). The incubated pancreatic tissue was washed with the same buffer, and digested with ColH at a final concentration of 0.1 mg/mL for more than 10 hours. The digested sample was divided into three aliquots (100 μL) in a 1.5 ml tube, and incubated with 10 μL stock solution (100 mM) of (N-Succinimidyloxycarbonylmethyl) tris (2,4,6-trimethoxyphenyl) phosphonium bromide (TMPP) (Sigma-Aldrich) in 50% acetonitrile for 30 min. Subsequently, samples were precipitated by cold

acetone (400 μL) and dried after centrifugation at 13,000 g. The dried samples were digested overnight by trypsin (10 μg/mL) in 100 mM ammonium bicarbonate solution.

The digested peptides were treated with a ZipTip (Millipore, Billerica, MA) for mass spectrometry. The peptide samples were loaded onto a 75-μm fused silica capillary column containing C18 resin. The peptides were eluted with an acetonitrile gradient (typically 2.5–40%) in 0.1% formic acid and analyzed by an LTQ Orbitrap XL mass spectrometer (Thermo Fisher Scientific Inc., Waltham, MA). The sample preparation and mass spectrometric analyses were performed in triplicate. Database searches of the NCBInr and SwissPlot databases were performed using the MASCOT ver. 2.4.00 search engine (Matrix Science, London, UK). MASCOT searches were done without protease specificity with a 5 ppm tolerance on the mass measurement in MS mode and 0.5 Da for MS/MS ions. Oxidation was considered as a variable modification for Met, Cys, Pro, and Lys. TMPP modification at the N-terminal was also taken into account. Protein identification was considered for MASCOT scores of $p < 0.05$.

Immunohistochemical analysis

Tissue was taken from the rat pancreas, fixed in 10% formalin onto slides for 10 minutes at room temperature and washed with phosphate-buffered saline (PBS) twice. Slides were pretreated with 10% rat serum for 30 minutes at room temperature to block endogenous peroxidase activity, followed by immunolabeling with primary antibodies against collagen I, II, III, or VI for 60 minutes at 37°C. Rabbit anti-Rat Collagen I (Monosan, Sanbio BV, Uden, Netherlands), anti-Collagen Type II (Chemicon, Merck Millipore, Darmstadt, Germany), anti-Collagen Type III (Chemicon), and anti-Collagen VI (Abcam, Cambridge, UK) antibodies were used. After washing the samples with PBS twice, secondary anti-rabbit antibodies conjugated to horseradish peroxidase (Dako, Glostrup, Denmark) were used, and antibody binding was localized with diaminobenzidine hydrochloride and samples were counterstained with hematoxylin.

Collagen digestion by collagenase subtype

Collagen digestion assays were performed using human Col-I (2.5 mg/mL), bovine Col-II (2.9 mg/mL), human Col-III (1.0 mg/mL), and human Col-VI (0.52 mg/mL) (BD Biosciences, Bedford, MA). Each collagen solution was mixed with an equal volume of buffer solution (100 mM HEPES (pH 8.0) and 1 mM $CaCl_2$), then digested by ColH or ColG (0.025 mg/mL) at 30°C. Digestion was stopped by adding sodium dodecyl sulfate (SDS) sample buffer at 5 and 10 min. and then samples were analyzed by SDS-polyaclylamidegel electrophoresis (PAGE).

Statistical analysis

All values were expressed as the means ± standard deviation (SD) and were analyzed using the Excel for Macintosh software program (Statcel3). Data from two groups were compared using Student's t-test. Data from three groups were compared using a single-factor analysis of variance (ANOVA). To use the ANOVA for multiple parameters, the Tukey-Kramer test was employed as a post-hoc test to determine the significant differences for pairwise comparisons. A value of $P < 0.05$ was considered to indicate statistical significance.

Results

The effects of the collagenase subtype on the yield and functions of isolated rat islets

In order to clarify the roles of ColG and ColH, the exact same lot and amount of TL was used in all the experimental groups. The islet yield in the GH group (ColG/ColH/TL) was the highest (4,101 ± 460 IEQs, n=9) among all the groups (Fig. 1A). In the H group (ColH/TL), a substantial number of well-shaped islets (2,811 ± 581 IEQs, n=9) were obtained following efficient dissociation of

pancreatic tissues, although a significant (~30%) decrease in the islet yield compared to the GH group was observed (p<0.001) (Fig. 1A). In the G group (ColG/TL), the pancreatic tissues were not dissociated at all, and no islets were retrieved (n=9) (Fig. 1A). The proportion of islet size was almost identical between the GH and H groups (Fig. 1B).

Regarding the *in vitro* functional assays using the isolated islets, no significant differences were detected between the GH and H groups in the ADP/ATP ratio (p=0.467, n=9) (Table 3), ATP/DNA (p=0.482, n=9) (Table 3), or insulin/DNA (p=0.991, n=9) (Table 3). Concerning the *in vivo* functional tests, no differences were detected between the GH and H groups in the blood glucose changes (Fig. 1C, D), AUC (p=0.978, n=6) (Table 3) and Kg values (p=0.847, n=6) (Table 3) in the IPGTT.

The effects of sequential injection of collagenase subtypes on the yield of isolated rat islets

To examine the role of the collagenase subtypes, ColG and ColH were sequentially injected into the pancreatic duct of rats. The islet yield was always highest when ColG and ColH were injected simultaneously. As shown in Fig. 2A, an additional injection of ColG following an initial injection of ColH led to a slight increase in the islet yield. On the contrary, no beneficial effects were observed following an additional injection of ColH (Fig. 2B).

Mass analysis of pancreatic tissues digested by ColH

Mass-analyzed peptide samples likely contain peptides digested by ColH, trypsin, and other pancreatic proteases, which were not perfectly denatured during the acetone precipitation process. The pancreatic tissue samples were labeled with TMPP after ColH digestion, because TMPP modification occurs at the N-terminal of the peptides (14) hydrolyzed by ColH. A database search was performed using the MASCOT software program (22) against non-specific peptides. The mass analyses detected 59-69 proteins (Table 4). Focusing on fibril proteins and TMPP-modified peptides, collagen-III (Col-

III) and collagen-I (Col-I) were included in the top 10 hits as search results (Fig. 3). Approximately 70% of the assigned peptides were TMPP-modified in Col-III and 25% were TMPP-modified in Col-I. Although a few TMPP modifications were also observed in other proteins with low search scores, the search result of these proteins included only one to four unique peptides, and the TMPP modification might have been accidental (Fig. 3).

Immunohistochemical analysis

All rat pancreatic sections showed positive labeling for all collagen subtypes examined (collagens I, II, III, and VI). As shown by representative examples (Fig. 4), the lobular and acinar septa, blood vessels, and the pancreatic ducts were positively stained for Col-I, III, and VI. In those areas, the staining for anti Col-I and VI was moderate, whereas that for Col-III was strong. Collagen II (Col-II) appeared to be diffusely located in the exocrine tissues. The peri-insular region displayed weak reactions for Col-II and III.

In vitro digestion of collagens by collagenase subtypes

Collagen digestions were performed with ColG or ColH, and the results were analyzed by SDS-PAGE (Fig. 5). Based on bands that appeared after digestion, neither ColG nor ColH was able to digest collagen-VI (Col-VI), which is a non-fibril collagen. ColG digested Col-I and III, however, less digestion was demonstrated for Col-II. In contrast, ColH digested all three fibril collagens tested (Col-I-III). Although Col-I and III were digested by both types of collagenase, different digestion patterns were observed, which was consistent with previous reports (10,11).

Discussion

Numerous studies have been performed to elucidate the roles of ColG and ColH during pancreatic islet isolation (1,9,18,32), but the results have been contradictory. One possible explanation is the enzyme blends used in those studies. In the present study, we examined the roles of ColG and ColH using highly-purified, TLA-free, enzyme blends. The innovative recombinant technique introduced in this study provides more accurate and highly reproducible outcomes compared with the conventional anion exchange chromatography technique (9,32). We have clearly shown that ColH and TL can efficiently dissociate rat pancreatic tissues and release functional islets from the acinar cells. In agreement with the present study, it was previously reported that ColH plays a predominant role in rat pancreas dissociation, while ColG has a limited role (32). In contrast, Brandhorst et al. reported that neither ColG nor ColH alone was able to dissociate pancreatic tissues and release islets from the exocrine tissue (9). This discrepancy may be explained, at least in part, by the method that Brandhorst et al. used, which employed a marginal amount of neutral protease to detect the optimal ratio between ColG and ColH. Based on these and the present results, the function of ColG may be partially replaced by neutral protease. Of particular interest, in the present study, no pancreatic tissues were dissociated by the combination of ColG and TL, suggesting that the function of ColH cannot be replaced by ColG and/or neutral protease. Moreover, it seems likely that some ECM components of the pancreatic tissues can be digested only by ColH. However, these findings are still limited in the case of small animal models, further studies in other species may be needed to draw broader conclusions.

An additional injection of ColG following an initial injection of ColH led to a slight increase in the islet yield. However, no beneficial effects were observed following an additional injection of ColH. These results suggest that ColH may need to bind to the target matrix components before ColG binds to them.

Since ColH was proven to be crucial for rat islet isolation in the present study, we also investigated the molecular composition of the target ECM of ColH using an immunohistochemical analysis and mass spectrometry. In the mass spectrometry assay, a protease inhibitor cocktail was added to the

pancreatic tissue before reacting them with ColH in order to prevent autolysis due to endogenous

digestive enzymes, such as trypsin and lipase. Both TMPP labeling and the use of the protease

inhibitor cocktail made it possible to narrow down the matrix components targeted by ColH. Mass

spectrometry suggested that ColH specifically reacts with Col-I and III, especially Col-III.

In the immunohistochemical analysis, both Col-I and III were located in the acinar septa and the

pancreatic ducts. Col-III was more intensely expressed in the exocrine area, while almost no

expression of Col-III was observed in peri-insular regions. This pattern was consistent with a previous

report by Van Deijnen et al (29). Furthermore, in support of the previous findings (20), the *in vitro*

digestion of collagens also revealed that Col-III was more effectively digested by ColH than by ColG.

Taken together, these findings suggest that islet isolation is initiated by fragmentation of the pancreatic

tissues by ColH mainly via the degradation of Col-I and III expressed on the exocrine tissues.

Thereafter, islets are released from the exocrine tissues, most likely by ColG and/or neutral protease.

Detecting the target matrix components of ColG and TL are topics of interests for a future study.

In conclusion, the present study revealed that ColH is of great importance, while ColG plays only a

supporting role, in rat islet isolation. In addition, the present data also suggest that one of the targets of

ColH is Col-III. Therefore, semiquantitation of the Col-III in pancreatic tissues may greatly contribute

to a more reproducible and successful islet isolation by optimizing the level of ColH. Further

investigations using a large animal model with highly variable matrix components (3,16,25,30) are

required.

Disclosure of conflict of interests

The authors state that they have no conflict of interest.

Contribution of each author

Kazutaka Murayama participated in the performance of the research and the writing of the paper

Youhei Yamagata participated in the performance of the research

Kimiko Watanabe participated in the writing of the paper

Takehiro Imura participated in the performance of the research

Akiko Inagaki participated in the performance of the research

Naomi Ohbayashi participated in the performance of the research

Hiroki Shima participated in the performance of the research

Satoshi Sekiguchi participated in the performance of the research